AFRL-RV-PS-
TR-2019-0003

USE OF AMBIENT NOISE GREEN'S FUNCTIONS IN EXPLOSION MOMENT TENSOR ESTIMATION (ANMT)

Douglas S. Dreger, et al.

University of California, Berkeley
215 McCone Hall
University of California
Berkeley, CA 94720

02 October 2018

Final Report

AIR FORCE RESEARCH LABORATORY
Space Vehicles Directorate
3550 Aberdeen Ave SE
AIR FORCE MATERIEL COMMAND
KIRTLAND AIR FORCE BASE, NM 87117-5776

DTIC COPY

NOTICE AND SIGNATURE PAGE

AFRL-RV-PS-TR-2019-0003 HAS BEEN REVIEWED AND IS APPROVED FOR PUBLICATION IN ACCORDANCE WITH ASSIGNED DISTRIBUTION STATEMENT.

//SIGNED//	//SIGNED//
Dr. Frederick Schult	Dr. Thomas R. Caudill, Chief
Program Manager/AFRL/RVBYE	AFRL Geospace Technologies Division

REPORT DOCUMENTATION PAGE

Form Approved
OMB No. 0704-0188

1. REPORT DATE *(DD-MM-YYYY)*	**2. REPORT TYPE**	**3. DATES COVERED** *(From - To)*
02-10-2018	Final Report	04 May 2016 – 30 Aug 2018

4. TITLE AND SUBTITLE
Use of Ambient Noise Green's Functions in Explosion Moment Tensor Estimation (ANMT)

5a. CONTRACT NUMBER
FA9453-16-C-0024

5b. GRANT NUMBER

5c. PROGRAM ELEMENT NUMBER
62601F

6. AUTHOR(S)
Douglas S. Dreger, Nathaniel J. Lindsey, and Sean Ford

5d. PROJECT NUMBER
1010

5e. TASK NUMBER
PPM00026922

5f. WORK UNIT NUMBER
EF129445

7. PERFORMING ORGANIZATION NAME(S) AND ADDRESS(ES)
University of California, Berkeley
215 McCone Hall
University of California
Berkeley, CA 94720

8. PERFORMING ORGANIZATION REPORT NUMBER

9. SPONSORING / MONITORING AGENCY NAME(S) AND ADDRESS(ES)
Air Force Research Laboratory
Space Vehicles Directorate
3550 Aberdeen Avenue SE
Kirtland AFB, NM 87117-5776

10. SPONSOR/MONITOR'S ACRONYM(S)
AFRL/RVBYE

11. SPONSOR/MONITOR'S REPORT NUMBER(S)
AFRL-RV-PS-TR-2019-0003

12. DISTRIBUTION / AVAILABILITY STATEMENT
Approved for public release; distribution is unlimited. (AFMC-2019-0061 dtd 04 Feb 2019)

13. SUPPLEMENTARY NOTES

14. ABSTRACT

We examine the use of ambient Noise Correlation Tensors (NCT) in seismic moment tensor inversion. We develop and test a new method, the Inversion of the Virtual Earthquake Approach (iVEA) based on the work published by Prieto and Beroza (2008) and Denolle et al. (2013), which introduced the forward problem, called the Virtual Earthquake Approach (VEA), in which complex wave propagation is captured in the NCT between seismometers using an ambient noise interferometry methodology, and then leveraged for use in ground motion estimation. The geometry is constrained by the common receiver in all NCTs (a virtual source) being located at the epicenter of the earthquake of interest. Further, VEA relies on spatial derivatives of surface wave eigenfunctions to convert the resulting set of unit-force surface-surface NCTs to a set of nine approximate dislocation source Green's Functions appropriate for modeling earthquakes and explosions, which we call the Green's Tensor (GT). We numerically investigate the terms used in this conversion (i.e., VEA), evaluate how the error in the conversion propagates into moment tensor solution uncertainty, assuming that the NCT perfectly retrieves the GT. Solutions obtained using iVEA and their uncertainties are evaluated in the context of the source-type discrimination application and then tested on real data. We find that while it is possible to use NCT to estimate seismic moment tensors, there are significant potential biases, and large uncertainties due to the approximate nature of the empirical NCT based Green's tensors. However, this approach does show some promise for using the ambient noise methodology to find Green's functions for complex wave propagation paths, which may allow data from those paths to be incorporated into a seismic moment tensor inversion in part. There is also promise in how iVEA enables the inversion of shorter period waveforms (f=0.1- 0.5 Hz) for regional distance moment tensor analysis than is commonly employed (f<0.1 Hz), but with that comes additional issues that can affect solution bias and uncertainty.

15. SUBJECT TERMS
seismic moment tensor, empirical Green's function, empirical Green's tensor, noise correlation tensor

16. SECURITY CLASSIFICATION OF:			**17. LIMITATION OF ABSTRACT**	**18. NUMBER OF PAGES**	**19a. NAME OF RESPONSIBLE PERSON**
a. REPORT	**b. ABSTRACT**	**c. THIS PAGE**			Dr. Frederick Schult
Unclassified	Unclassified	Unclassified	Unlimited	52	**19b. TELEPHONE NUMBER** *(include area code)*

This page is intentionally left blank.

Table of Contents

List of Figures

Acknowledgments

The authors would like to thank a number of individuals for their efforts. Roland Gritto deployed and recorded the broadband seismometer data used in this study's application at The Geysers. Collaboration with Avinash Nayak and Sierra Boyd and Taka'aki Taira improved the direction and content of this study. Avinash Nayak wrote the source-type inversion code used in this work. Aurelie Guilhem and Andrea Chiang wrote some of the visualization scripts used to generate a few of the figures.

1. SUMMARY

In this project (FA9453-16-C-0024) we build on our earlier results (DE-FC52-06NA27324, Dreger et al., 2008; Ford et al., 2012; Ford et al., 2010; Ford et al., 2009ab; Ford et al., 2008, Ford 2008; FA9453-10-C-0263, Chiang et al., 2014, Nayak and Dreger, 2014, Chiang et al., 2018; FA9453-13-C-0271, Chiang 2015, Chiang et al., 2016, Nayak and Dreger, 2015) to examine the use of ambient Noise Correlation Tensors (NCT), e.g. Green's functions, in seismic moment tensor inversion. We develop and test a new method that we call the Inversion of the Virtual Earthquake Approach (iVEA). This method is based on the work published by Prieto and Beroza (2008) and Denolle et al. (2013), which introduced the forward problem, called the Virtual Earthquake Approach (VEA), in which complex wave propagation is captured in the NCT between seismometers using an ambient noise interferometry methodology, and then leveraged for use in ground motion estimation. The geometry is constrained by the common receiver in all NCTs (a virtual source) being located at the epicenter of the earthquake of interest. Further, VEA relies on spatial derivatives of surface wave eigenfunctions to convert the resulting set of unit-force surface-surface NCTs to a set of nine approximate dislocation source Green's Functions appropriate for modeling earthquakes and explosions, which we call the Green's Tensor (GT). In Section 3.1 we start to develop iVEA by first numerically investigating the terms used in this conversion (i.e., VEA). In Section 3.2, we continue to develop iVEA by evaluating how the error in the conversion propagates into moment tensor solution uncertainty, assuming that the NCT perfectly retrieves the GT. Solutions obtained using iVEA and their uncertainties are evaluated in the context of the source-type discrimination application (e.g. Ford et al., 2009a). In Section 3.3, we test iVEA on real data. We investigate the best method to compute the absolute NCT from continuous recordings of ambient noise for the study region, and we utilize ambient noise recordings and earthquake records (M2.87; z=1.5 km) from broadband stations deployed in The Geysers Geothermal Field in Northern California in 2012 – 2013. We find that while it is possible to use NCT to estimate seismic moment tensors there are significant potential biases, and large uncertainties due to the approximate nature of the empirical NCT based Green's tensors. However, this approach does show some promise for using the ambient noise methodology to find Green's functions for complex wave propagation paths, which may allow data from those paths to be incorporated into a seismic moment tensor inversion in part. There is also promise in how iVEA enables the inversion of shorter period waveforms (f=0.1- 0.5 Hz) for regional distance moment tensor analysis than is commonly employed (f<0.1 Hz), but with that comes additional issues that can affect solution bias and uncertainty. We summarize our results and discuss future directions of iVEA in Section 4.

2. INTRODUCTION

A common way to study the seismogenic process is to represent the source as an infinitesimal point source comprised of force couples and dipoles acting at the seismic event's origin. The summation of these force couples and dipoles are related to the radiation pattern of seismic energy, which is commonly represented as a seismic moment tensor (Gilbert, 1973). Records of the seismic event (time series data) are modeled using a moment tensor convolved with a set of Green's functions for an appropriately calibrated velocity model. Moment tensor inversion has been applied to a wide array of Earth processes including earthquakes, underground cavity collapse, nuclear explosion, volcano deformation events, high temperature fluid-rock interactions, and ice calving, among many others (Dziewonski et al., 1981; Dreger et al., 1993, Dreger and Woods 2002, Minson and Dreger 2008, Ford et al., 2008; Ford et al. 2009b, Walter et al., 2009, Ekstrom et al., 2012; Duputel et al., 2012; Heeszel et al., 2013, Nayak and Dreger, 2014, 2018, Boyd et al., 2015, Vavryčuk, 2015, Alvizuri et al., 2018; see review by Julian et al., 1998, Miller et al., 1998).

Because seismic records are the mathematical convolution of a source model (moment tensor) and an Earth model (Green's tensor), source physics studies become untenable in the face of complex or poor velocity model information. Moment tensor inversion is therefore typically carried out at low frequencies (f<0.1 Hz) for moderate to large seismic events (Mw>3.5) when using data recorded at regional distances from the seismic event (10's – 100's km); large wavelengths are insensitive small scale structural heterogeneity, thus it is valid to use an approximate 1-D velocity model to describe wave propagation. This strategy has proven to be very effective, however it is sometimes necessary to avoid the use of particular station paths in cases where large 3-D wave propagation components become critically important. As the magnitude of the earthquake decreases, the amplitude level of low frequency seismic energy decreases below the background noise, necessitating the use of higher frequency waves, which are more sensitive to small scale structural heterogeneity of the Earth, and for which simple velocity models may not be appropriate. One consequence of this problem is that field campaign studies of small magnitude seismogenic processes (e.g., microearthquake source studies in volcanic and geothermal settings) must deploy high numbers of seismometers over very local distances (<20 km). Some studies have attempted to use 3-D Green's functions to invert for the moment tensor (e.g. Covellone and Savage, 2012, Chiang 2015, Nayak and Dreger, 2018). However, the ability to confidently obtain a seismic moment tensor solution taking into account complete 3D wave propagation effects is only as good as the suitability of the approximate 3D velocity models used to correct for propagation effects.

The field of ambient noise seismology is based on a data processing methodology that retrieves empirical estimates of the true Green's function between any two passively recording seismometer components as if one receiver is a unit-force source that is recorded at the other station (Shapiro and Campillo; 2004, Snieder, 2004). Recent studies involving the ambient seismic wavefield, which is dominated by surface waves, have made Rayleigh and Love wave phase and group velocity measurements across many scales to resolve subsurface heterogeneity and detect structural changes (Lin et al., 2008; Brenguier, et al., 2008a,b; James et al., 2017; Lin et al., 2013; Zhan et al., 2013). Ambient noise seismology studies have been able to accurately model wave propagation through Earth structure at relatively high frequencies (f<0.5 Hz) over larger path lengths. If each of the two recording seismometers is a 3C station, then there exist nine combinations of sensor components, which results in the rank two noise correlation tensor (NCT)

of radial, transverse and vertical component pairs. The NCT is equal to the true unit-force Green's tensor if and only if the noise source field is omnidirectional, equipartitioned, and stationary over the period of observation (Wapenaar et al., 2010). In practice, dozens of studies have demonstrated that this assumption is never fully realized, despite the fact that stacking ambient noise cross-correlation signals over long time results in a stable recovery of the NCT. The best practice for how to perform the ambient noise interferometry and stack the signals is an area of active research (e.g. Sheng et al., 2017; Sager et al., 2018) and the results suggest that an optimal workflow for a given region and station configuration needs to be evaluated, and tuned. Thus one part of the present research was to investigate different interferometry methods for the application to actual earthquake data. To date, issues related to ambient source field non-stationarity have largely preempted the use of true amplitude information carried by the ambient seismic field (Prieto and Beroza, 2008; Prieto et al., 2011; Lawrence and Prieto, 2011; Tsai, 2011; Stehly and Boue, 2017), but the relative GF amplitudes across the NCT for a single station pair path have been employed to study seismic attenuation (Prieto and Beroza, 2008; Lin et al., 2013; Prieto et al., 2011; Lawrence et al., 2011; Sheng et al., 2017; Viens et al., 2017; Kwak et al., 2017), ground-shaking infrastructure hazard (Prieto et al., 2010), and discriminate between 1-D and 3-D propagation paths (Nayak et al., 2017).

Denolle et al. (2013) was the first to recognize that the noise correlation tensor (NCT) representing the surface-to-surface unit-force source Green's functions could be converted to an approximate earthquake-focal-depth-to-surface dislocation source Green's tensor (GT) using the theoretical form for the fundamental mode surface-wave displacement eigenfunctions, a method that they refer to as the Virtual Earthquake Approach (VEA). VEA essentially applies spatial derivatives to generate dislocation source functions (couples and dipoles), and projects the surface motions to depth assuming the theoretical form of fundamental mode Love and Rayleigh waves for a unit-force excitation to develop a corrective filter that is applied to the NCT in the frequency domain. The station geometry for VEA applications is constrained by the requirement that there must be one common receiver to develop all station pair NCTs (i.e., the virtual source), and this common receiver must lie at or near the epicenter of the earthquake of interest. The VEA also requires that some velocity model information exists a priori, because one must be able to compute spatial derivatives of surface wave eigenfunctions, described in the following section, in order to make the NCT-GT conversion possible.

The development of VEA may be important for moment tensor studies because the NCT captures relatively high frequency regional wave propagation information, which is classically been a large source of uncertainty for moment tensor inversion at higher frequencies and regional distances, such as for studies involving microearthquake events. In this work we develop and test a new method that we call the Inversion of the Virtual Earthquake Approach (iVEA; see Figure 1).

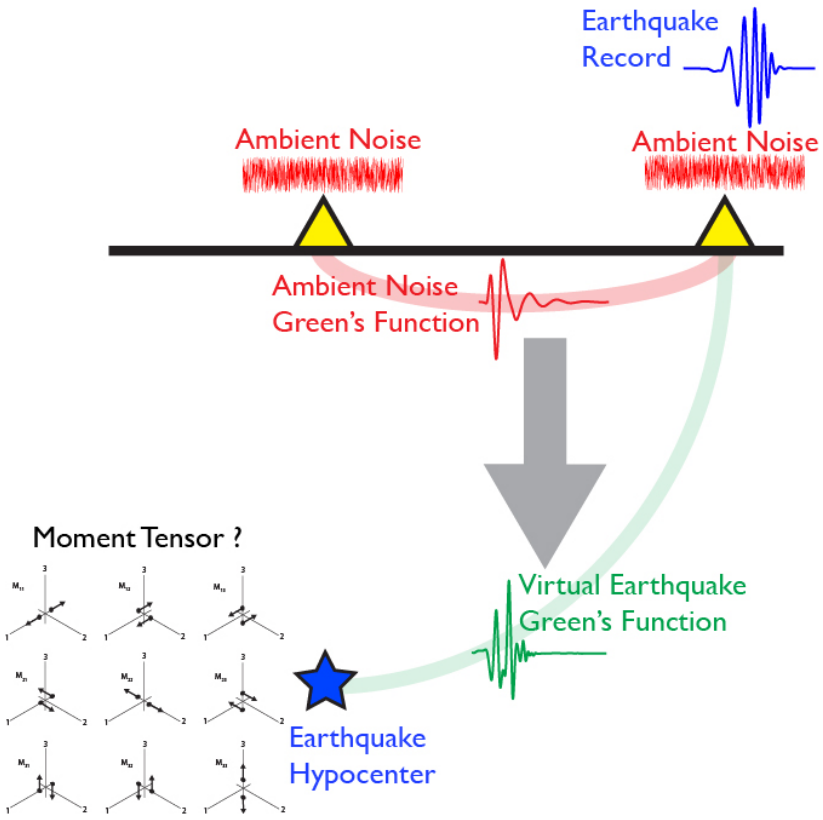

Figure 1. Concept of the Inversion with the Virtual Earthquake Approach (iVEA). *Ambient noise recordings (red waveforms) are used to estimate approximate sets of hypocenter-surface Green's tensors (green waveforms) between a common epicentral virtual source and an array of seismometers. In this paper we invert earthquake seismic records (blue waveform) using the Virtual Earthquake Approach for the six elements of the full moment tensor (black arrows).*

3. METHODS, ASSUMPITONS, AND PROCEDURES: THE VIRTUAL EARTHQUAKE APPROACH AND ITS UNCERTAINTY

The Virtual Earthquake Approach and its Uncertainty

3.1. Introduction

Denolle et al. (2013) was the first to recognize that the noise correlation tensor (NCT) representing the surface-to-surface unit-force source Green's functions could be converted to an approximate earthquake-focal-depth-to-surface dislocation source Green's tensor (GT) using the theoretical form for the fundamental mode surface-wave displacement eigenfunctions, a method that they refer to as the Virtual Earthquake Approach (VEA). VEA essentially applies spatial derivatives to generate dislocation source functions (couples and dipoles), and projects the surface motions to depth assuming the theoretical form of fundamental mode Love and Rayleigh waves for a unit-force excitation to develop a corrective filter that is applied to the NCT in the frequency domain. Since its introduction in 2013, VEA has been utilized in a forward modeling sense to understand ground motion hazard in various contexts, including moderate to large magnitude (Mw 4.2-7) at crustal depths (5 - 15 km), with strike-slip and reverse mechanisms (Denolle et al., 2013; Denolle et al., 2014a; Viens et al., 2015). Other studies, including Viens et al. (2014) and Kwak et al. (2017), have appealed to the VEA concept, but do not actually apply the VEA corrections. Previous applications demonstrate that VEA captures some information about surface wave excitation. This information is extracted in the primary and secondary ocean-solid Earth microseism source bands ($f \sim 0.02 – 0.5$ Hz), which leads to one key advantage of VEA being ground motion predictions at relatively high frequencies up to 0.5 Hz. This is important because such high frequency ground motions are subject to significant 3D wave propagation effects, which are difficult to capture using synthetic ground motion modeling methods. VEA has been shown to provide good prediction of the seismic ground motion hazard in complex sedimentary basin environments in terms of peak ground acceleration or velocity (Denolle et al., 2013, 2014b).

In Denolle et al. (2013), the authors found good agreement between earthquake time histories and VEA predicted ground motions, and they interpreted the major discrepancies as being the result of non-stationarity of the ambient noise source field. However, alternative explanations posit that the proposed VEA fundamental mode eigenfunction-based filter does not account for off-great-circle propagation, surface wave to surface wave conversions, body wave to surface wave conversions, or medium anisotropy. These real wave propagation effects may be present in the NCT, however the simplified corrective functions are based on the theoretical form for fundamental mode surface waves in 1-D layered, isotropic media. To our knowledge, the valid range of VEA and the related uncertainties have not been documented. In Sections 3.1 and 3.2 we investigate these uncertainties in the NCT and how they propagate to uncertainties in the derived moment tensor source parameters.

Additional biases due to how VEA is applied in practice may also be important, such as the source depth, the source type, lateral offset between the true epicenter and the virtual source, the suitability of the simple velocity model used to compute the eigenfunctions, and how the vertical derivatives of the eigenfunctions are calculated. At the outset of the work, we recognized that these potential errors introduced by the ambient noise source field and the approximate corrective filters can be problematic for the forward estimation of ground motions, and more so in using NCT to invert for

seismic source parameters of earthquakes and explosions. In addition, there are a variety of approaches for estimating the NCT, and within each approach considerable leeway on how to perform the calculations. This is a current area of research and new methods are being tested to improve the accuracy of ambient noise processing (Sheng et al., 2017; Sager et al., 2018). Thus in Section 3.3 we discuss how we approximate the NCT, and compare results for two methods.

3.2 Theory of the Virtual Earthquake Approach

The far-field earthquake displacement field is described by the time-domain convolution or Fourier domain product of the spatial derivatives of the second rank, nine-element Green's Tensor and a point-source, represented by a moment tensor M_{pq}, whose elements weight the components of the Green's Tensor (Aki and Richards, 2002, Eqn 3.23):

$$u_i(r,z,t) = M_{pq} * \frac{\partial}{\partial q} G_{ip}(r,z,t) \quad \text{1a}$$

$$\hat{u}_i(r,z,\omega) = M_{pq} \frac{\partial}{\partial q} \hat{G}_{ip}(r,z,\omega), \quad \text{1b}$$

where ω is the frequency of interest, and subscripts *i, p* and *q* represent the ground motion component, the direction of the unit-force, and the direction that the spatial derivative is applied. G_{ip} are the unit-force Green's function on the ith component for a force in the pth direction. The ^ symbol in all equations symbolizes the Fourier Domain representation of the quantity, meaning operations are on complex Fourier spectra. In practice *i* and *p* are defined as one of radial (R), tangential (T), and down (D), where for example G_{RD} corresponds to the "Radial" response to a vertical "Down" unit force. We choose to explicitly describe the source-receiver geometry in the horizontal (r) and vertical (z) dimensions in order to clarify the operations and assumptions that follow. After rotation from a North-East-Down (NED) Cartesian coordinate reference frame into a Radial-Transverse-Down (RTD) cylindrical coordinate reference frame oriented in the plane of the source and the receiver, if we can assume that G_{ip} is dominated by fundamental mode Love (G_{ip}^{L}) and Rayleigh (G_{ip}^{R}) waves, then the Green's Tensor has five non-zero Green's Functions:

$$\hat{G}_{ip} = \hat{G}_{ip}^{L} + \hat{G}_{ip}^{R} = \begin{pmatrix} \hat{G}_{RR} & 0 & \hat{G}_{RD} \\ 0 & \hat{G}_{TT} & 0 \\ \hat{G}_{DR} & 0 & \hat{G}_{DD} \end{pmatrix} \quad 2$$

of the form of Eqn 7.146 and 7.147 from Aki and Richards (2002):

$$\hat{G}_{ip}^{L}(r,z,\omega) = \frac{1}{8c_L U_L I_1} \sqrt{\frac{2}{\pi k_L r}} \begin{pmatrix} 0 & 0 & 0 \\ 0 & L_1(z,\omega)L_1(0,\omega) & 0 \\ 0 & 0 & 0 \end{pmatrix} e^{ik_L r + i\frac{\pi}{4}} \quad 3$$

$$\hat{G}_{ip}^{R}(r,z,\omega) = \frac{1}{8c_R U_R I_1} \sqrt{\frac{2}{\pi k_R r}} \begin{pmatrix} R_1(z,\omega)R_1(0,\omega) & 0 & -iR_1(z,\omega)R_2(0,\omega) \\ 0 & 0 & 0 \\ iR_2(z,\omega)R_1(0,\omega) & 0 & R_2(z,\omega)R_2(0,\omega) \end{pmatrix} e^{ik_R r + i\frac{\pi}{4}} \quad 4$$

The terms that are zero in (2) are cross terms involving excitation in the P-Sv coordinates with recording on the transverse component, or vice versa. When inspecting a NCT, if these components were non-zero that would be evidence of 3-D multipathing of the ambient noise field. They are not considered in the development of the corrective filters that follow.

Re-writing the separate Green's Functions we have:

$$\hat{G}_{TT}(r,z,\omega) = \frac{1}{8c_L U_L I_1}\sqrt{\frac{2}{\pi k_L r}}L_1(z,\omega)L_1(0,\omega)e^{ik_L r + i\frac{\pi}{4}} \quad 5a$$

$$\hat{G}_{RR}(r,z,\omega) = \frac{1}{8c_R U_R I_1}\sqrt{\frac{2}{\pi k_R r}}R_1(z,\omega)R_1(0,\omega)e^{ik_R r + i\frac{\pi}{4}} \quad 5b$$

$$\hat{G}_{RD}(r,z,\omega) = -i\frac{1}{8c_R U_R I_1}\sqrt{\frac{2}{\pi k_R r}}R_1(z,\omega)R_2(0,\omega)e^{ik_R r + i\frac{\pi}{4}} \quad 5c$$

$$\hat{G}_{DR}(r,z,\omega) = i\frac{1}{8c_R U_R I_1}\sqrt{\frac{2}{\pi k_R r}}R_2(z,\omega)R_1(0,\omega)e^{ik_R r + i\frac{\pi}{4}} \quad 5d$$

$$\hat{G}_{DD}(r,z,\omega) = \frac{1}{8c_R U_R I_1}\sqrt{\frac{2}{\pi k_R r}}R_2(z,\omega)L_2(0,\omega)e^{ik_R r + i\frac{\pi}{4}} \quad 5e$$

The surface wave displacement eigenfunctions (L_1, R_1, R_2) are solutions to the wave equation subject to a free surface boundary condition, determined, for example analytically using the Haskell-Thompson propagator matrix method (Herrmann, 1978). These terms are frequency and depth dependent. The terms c, U, and k are the frequency-dependent phase velocity, group velocity, and wavenumber, with subscripts of "R" and "L" for Rayleigh and Love waves, respectively. The first energy integral is defined as: $I_1 = \frac{1}{2}\int_0^\infty \rho(z)(R_1(z)^2 + R_2(z)^2)dz$. The fundamental mode surface wave assumption described in (4) does not account for body waves, surface wave to surface wave and body wave to surface wave conversions, off-great-circle propagation and the related scattering effects, anisotropy, and higher mode surface waves.

To calculate the displacement field in (1) using a known moment tensor, one must differentiate (5) with respect to its spatial dimensions. To do this, Aki and Richards (2002) assumed that the largest contributions to u_i come from the vertical derivatives of $L_1(z, \omega)$, $R_1(z, \omega)$, and $R_2(z, \omega)$ and the horizontal derivatives of $e^{-ik_R r}$ and $e^{-ik_L r}$. This simplification can be thought of as a linear filter applied to the Green's Functions that both incorporates the moment tensor scaling and converts from unit-force to force-couple. Expanding (1) in an RTD reference frame, the resulting displacement field simplifies to:

$$\hat{u}_T(r,z,\omega) \approx (ik_L M_{TR} + \frac{\partial L_1(z)}{\partial z}M_{TD})\hat{G}_{TT}(r,z,\omega) \quad 6a$$

$$\hat{u}_T(r,z,\omega) \approx \left(ik_R M_{DR} + \frac{\partial R_2(z)}{\partial z}M_{DD}\right)\hat{G}_{RD}(r,z,\omega) + \left(ik_R M_{RR} + \frac{\partial R_1(z)}{\partial z}M_{RD}\right)\hat{G}_{RR}(r,z,\omega) \quad 6b$$

$$\hat{u}_D(r,z,\omega) \approx \left(ik_R M_{RR} + \frac{\partial R_1(z)}{\partial z} M_{RD}\right)\hat{G}_{DR}(r,z,\omega) + \left(ik_R M_{DR} + \frac{\partial R_2(z)}{\partial z} M_{DD}\right)\hat{G}_{DD}(r,z,\omega) \quad 6c$$

Following Aki and Richards (2002) and Prieto and Beroza (2008), Denolle et al. (2013) observed that for a 1-D homogeneous velocity model the Green's Functions at depth (z) and at the surface (z=0) are linearly related through the ratio of the respective surface wave eigenfunctions:

$$\hat{G}_{TT}(r,z,\omega) = \frac{L_1(z)}{L_1(0)}\hat{G}^A_{TT}(r,0,\omega) \quad 7a$$

$$\hat{G}_{RR}(r,z,\omega) = \frac{R_1(z)}{R_1(0)}\hat{G}^A_{RR}(r,0,\omega) \quad 7b$$

$$\hat{G}_{RD}(r,z,\omega) = \frac{R_2(z)}{R_2(0)}\hat{G}^A_{RD}(r,0,\omega) \quad 7c$$

$$\hat{G}_{DR}(r,z,\omega) = \frac{R_1(z)}{R_1(0)}\hat{G}^A_{DR}(r,0,\omega) \quad 7d$$

$$\hat{G}_{DD}(r,z,\omega) = \frac{R_2(z)}{R_2(0)}\hat{G}^A_{DD}(r,0,\omega) \quad 7e$$

Replacing the Green's Functions shown in (6) with the converted surface Green's Functions described in (7), Denolle et al. (2013) thus proposed[1] the Virtual Earthquake Approach in which an epicenter-to-surface, unit-force ambient noise Green's Tensor (G^A_{ip}) can be directly related to the hypocenter-to-surface, dislocation Green's tensor (G_{ip}) through a linear filter.

In essence, VEA replaces (1) by:

$$\hat{u}_i(r,0,\omega) = M_{pq}\hat{F}\hat{G}^A_{ip}(r,0,\omega) \quad 8$$

which can be expanded component-wise to show that F depends only on surface waves information, more specifically the surface wave wavenumber-frequency relationships, surface wave displacement eigenfunctions, and vertical derivatives of surface wave displacement eigenfunctions:

$$\hat{u}_T(r,0,\omega) \approx (ik_L \frac{L_1(z)}{L_1(0)} M_{TR} + \frac{1}{L_1(0)}\frac{\partial L_1(z)}{\partial z} M_{TD})\hat{G}^A_{TT}(r,0,\omega) \quad 9a$$

$$\hat{u}_R(r,0,\omega) \approx \left(ik_R \frac{R_2(z)}{R_2(0)} M_{DR} + \frac{1}{R_2(0)}\frac{\partial R_2(z)}{\partial z} M_{DD}\right)\hat{G}^A_{RD}(r,0,\omega)$$

$$+ \left(ik_R \frac{R_1(z)}{R_1(0)} M_{RR} + \frac{1}{R_1(0)}\frac{\partial R_1(z)}{\partial z} M_{RD}\right)\hat{G}^A_{RR}(r,0,\omega) \quad 9b$$

$$\hat{u}_D(r,0,\omega) \approx \left(ik_R \frac{R_1(z)}{R_1(0)} M_{RR} + \frac{1}{R_2(0)}\frac{\partial R_1(z)}{\partial z} M_{RD}\right)\hat{G}^A_{DR}(r,0,\omega)$$

[1]Here we correct a sign error made in the original VEA equations, see next page for details.

$$+\left(ik_R \frac{R_2(z)}{R_2(0)} M_{DR} + \frac{1}{R_1(0)} \frac{\partial R_2(z)}{\partial z} M_{DD}\right) \hat{G}^A_{DD}(r,0,\omega) \quad 9c$$

Note that *F* does not account for off-great-circle propagation, surface-wave-to-surface-wave conversions, body-wave-to-surface-wave conversions, or anisotropy, any of which may be present in the ambient noise Green's Tensor.

Errors in Original Virtual Earthquake Approach Equations

During implementation, we identified a critical sign error[2] in the formulae of Denolle et al., (2013). In an RTD coordinate reference frame, all terms should be positive. We re-write the original and corrected equations below for clarity.

Original VEA Equations (Denolle et al., 2013):

$$\hat{u}_T(r,0,\omega) \approx -ik_L \frac{L_1(z)}{L_1(0)} \hat{G}^A_{TT}(r,0,\omega) M_{TR} + \frac{1}{L_1(0)} \frac{\partial L_1(z)}{\partial z} \hat{G}^A_{TT}(r,0,\omega) M_{TD} \quad 9a$$

$$\hat{u}_R(r,0,\omega) \approx -ik_R \frac{R_2(z)}{R_2(0)} \hat{G}^A_{RD}(r,0,\omega) M_{DR} + \frac{1}{R_2(0)} \frac{\partial R_2(z)}{\partial z} \hat{G}^A_{RD}(r,0,\omega) M_{DD}$$
$$-ik_R \frac{R_1(z)}{R_1(0)} \hat{G}^A_{RR}(r,0,\omega) M_{RR} + \frac{1}{R_1(0)} \frac{\partial R_1(z)}{\partial z} \hat{G}^A_{RR}(r,0,\omega) M_{RD} \quad 9b$$

$$\hat{u}_D(r,0,\omega) \approx -ik_R \frac{R_1(z)}{R_1(0)} \hat{G}^A_{ZD}(r,0,\omega) M_{RR} + \frac{1}{R_1(0)} \frac{\partial R_1(z)}{\partial z} \hat{G}^A_{ZD}(r,0,\omega) M_{RD}$$
$$-ik_R \frac{R_2(z)}{R_2(0)} \hat{G}^A_{DD}(r,0,\omega) M_{DR} + \frac{1}{R_2(0)} \frac{\partial R_2(z)}{\partial z} \hat{G}^A_{DD}(r,0,\omega) M_{DD} \quad 9c$$

Corrected VEA Equations (Aki and Richards, 2002; this publication):

$$\hat{u}_T(r,0,\omega) \approx ik_L \frac{L_1(z)}{L_1(0)} \hat{G}^A_{TT}(r,0,\omega) M_{TR} + \frac{1}{L_1(0)} \frac{\partial L_1(z)}{\partial z} \hat{G}^A_{TT}(r,0,\omega) M_{TD} \quad 10a$$

$$\hat{u}_R(r,0,\omega) \approx ik_R \frac{R_2(z)}{R_2(0)} \hat{G}^A_{RD}(r,0,\omega) M_{DR} + \frac{1}{R_2(0)} \frac{\partial R_2(z)}{\partial z} \hat{G}^A_{RD}(r,0,\omega) M_{DD}$$
$$+ik_R \frac{R_1(z)}{R_1(0)} \hat{G}^A_{RR}(r,0,\omega) M_{RR} + \frac{1}{R_1(0)} \frac{\partial R_1(z)}{\partial z} \hat{G}^A_{RR}(r,0,\omega) M_{RD} \quad 10b$$

$$\hat{u}_D(r,0,\omega) \approx ik_R \frac{R_1(z)}{R_1(0)} \hat{G}^A_{DR}(r,0,\omega) M_{RR} + \frac{1}{R_1(0)} \frac{\partial R_1(z)}{\partial z} \hat{G}^A_{DR}(r,0,\omega) M_{RD}$$
$$+ik_R \frac{R_2(z)}{R_2(0)} \hat{G}^A_{DD}(r,0,\omega) M_{DR} + \frac{1}{R_2(0)} \frac{\partial R_2(z)}{\partial z} \hat{G}^A_{DD}(r,0,\omega) M_{DD} \quad 10c$$

3.3 Methodology

To understand the theoretical bias of the VEA approximation for ground motion estimates in a forward sense, we compared the synthetic ground motion displacement time series computed using

[2]We also noted a minor typographical error in the original VEA equations: G_{ZD} should be G_{DR}.

the exact hypocentral depth GT with the synthetic displacement computed using the VEA estimate of the GT. We aim study how the error introduced in the surface-to-depth conversion of the NCT to the GT is affected by source depth and source type. To isolate this uncertainty, we first computed an ideal NCT (true GT) for a surface focus (z=0.050 km depth) unit-force source using the frequency-wavenumber integration code in Computer Programs in Seismology 3.30 (Herrmann, 2013). We used a radial distance of 100 km with the simple 1-D velocity model shown in Figure 2a. The velocity model is commonly used to represent the crust in Northern California. We calculate 1024 points in each Green's function sampled at 0.25 seconds to include information up to 2 Hz (Nyquist frequency). CPS3.30 was also used to compute fundamental-mode surface wave displacement eigenfunctions using the surface wave synthetic code. These eigenfunctions and the vertical derivatives of these eigenfunctions were used to convert the ideal NCT to the ideal hypocentral focused GT using (10) above for a given source type. We also computed the true ground motion displacement using the frequency-wavenumber integration code for a hypocentral depth GT of the known source type.

In order to take a vertical derivative of the eigenfunctions, we discretized the velocity model shown in Figure 2a into many layers of z=0.25 km thickness when executing CPS3.30. Prior to taking the derivative we smoothed the eigenfunctions with a cubic spline interpolation method in Matlab. Values of the eigenfunctions and associated vertical derivatives in the frequency domain, shown in Figure 2b, were then chosen to coincide with the frequencies present in the Fourier spectra of the NCT. Figure 3 shows the Love and Rayleigh wave phase velocity dispersion relationship, which is used in the operations of equation (10).

The results of this test for a pure double-couple source (strike=23^o, rake=45^o, dip=67^o) at variable depth are shown in Figure 4. The error associated with the VEA approximation is found to increase with depth. This is because the fundamental mode surface wave sensitivity kernels decrease to zero at large depth. This depends on the velocity model structure. Layers are also expected to play a role, thus VEA will work differently in different models.

Figure 4c and 4d compares exact and approximate transverse component displacements for increasing depth with a pure double-couple source (strike=23^o, rake=45^o, dip=67^o) and a source-receiver geometry of 100 km lateral offset and 20^o azimuth. The approximate displacement records are well-behaved, specifically at shallow depths (z<2.5 km) and during the surface wave portion of the waveform. It is observed, not surprisingly, that the mismatch between the actual dislocation source synthetics (black) and the synthetics constructed with filtered unit-force Green's functions (red) increases with increasing depth. It is somewhat surprising that the low-frequency body wave portion of the record is reasonably well approximated even though the theory is for only fundamental mode surface waves. At deeper depths the agreement between the body wave portion of the record completely breaks down and there are noticeable differences in the amplitude and phase of the surface waves. The errors also appear to increase with frequency, however in fact the low and high frequency surface waves behave equally well. The VEA conversion is based on the fundamental mode surface wave eigenfunctions, and thus relatively high frequency body wave terms introduce a large misfit during VEA conversion specifically during the portion of the displacement time history when the body wave arrives. The behavior of radial and vertical component records is the same as for the transverse component.

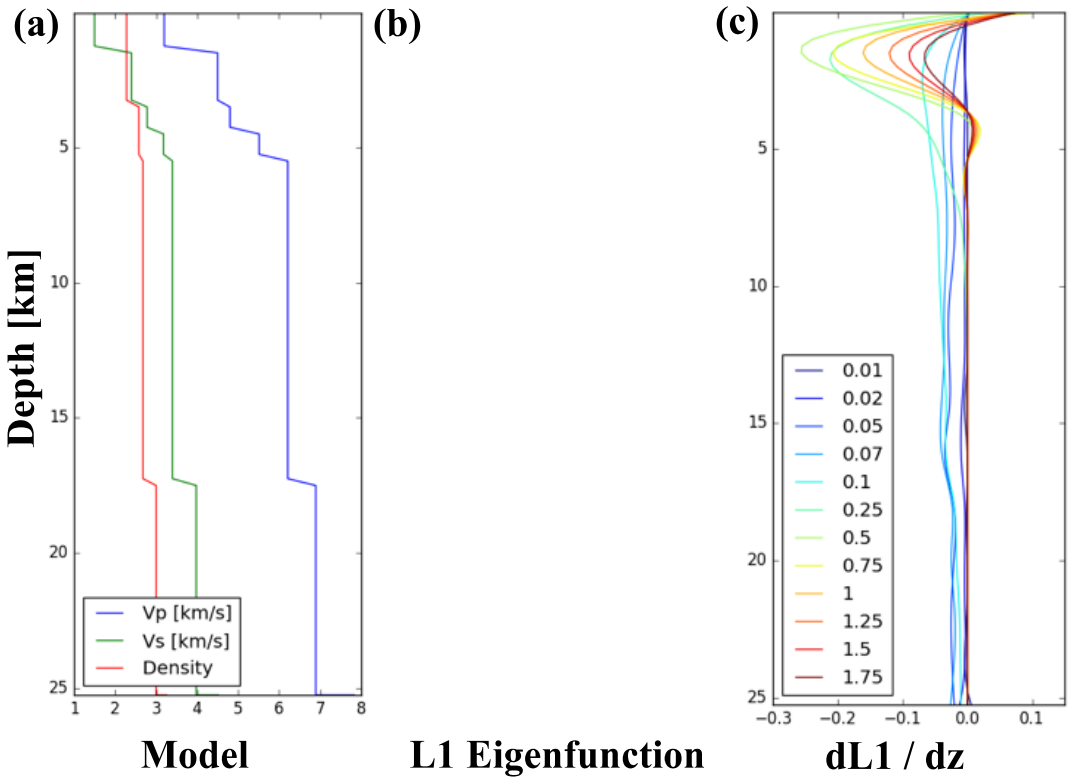

Figure 2 (left) Model parameters used in frequency-wavenumber integration to compute dispersion eigenfunctions corresponding to Love (center) and Rayleigh wave (not shown) excitation over a range of frequency and depth Vertical derivatives of L1 (right) Vertical derivatives of L1 after application of the smoothing procedure.

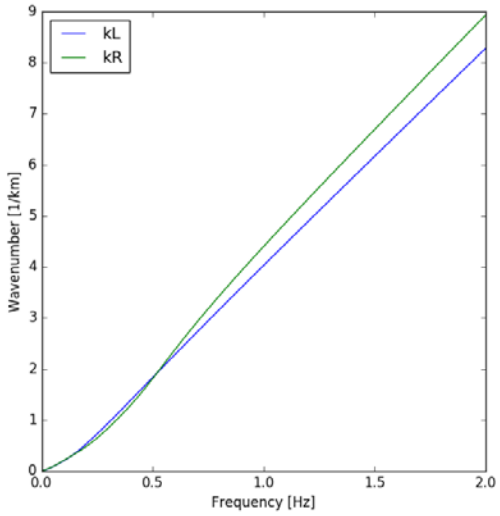

Figure 3 Dispersion relationship for the velocity model parameters shown in Figure 2.

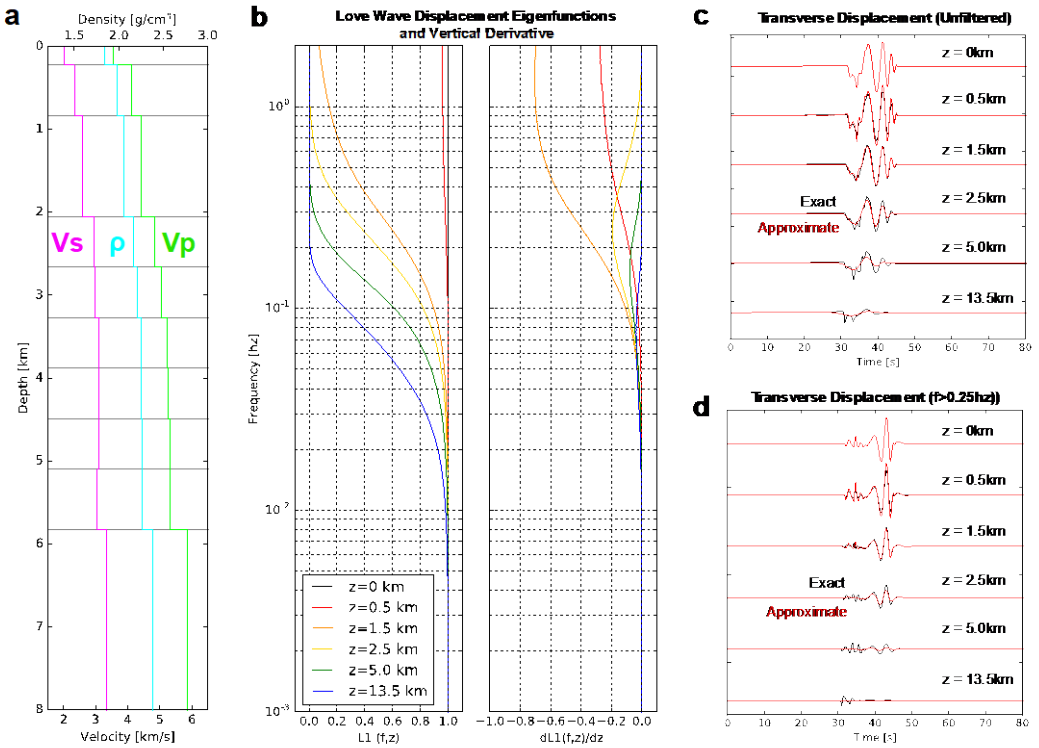

Figure 4 (a) Velocity model (b) Fundamental mode Love wave eigenfunctions (left) and vertical derivatives (right) for various depths, which are used to convert a surface ambient noise Green's tensor to an approximate buried earthquake Green's tensor. (c) Approximate [red] and exact [black] seismograms for various source depths show the errors introduced at 100 km path at an azimuth of 20 degrees for double-couple (strike/rake/dip=23/45/67 degrees) moment tensor. (d) Same as (c) but with a high-pass filter applied to the result (f>0.25 Hz).

3.4 Conclusions

We have reviewed the published VEA approach and corrected an error in the formulation. We have developed MatLab and Python code to perform the filtering operations to convert NCT to GT using the Herrmann (2013) Computer Programs for Seismology 3.30 code to calculate the surface wave vertical excitation functions. Herrmann's (2013) frequency-wavenumber integration code was used to compute surface-focus unit-force Green's functions and buried-source dislocation-source/force-couple Green's functions for a comparative analysis to test the approximate spatial derivative and focal depth projection filters. We find that at lower frequency the surface wave and even the body wave portion of the records are well matched by the filtered synthetic NCT. The agreement is observed to decrease with increasing source depth, as anticipated. This synthetic comparison suggest that the filtered NCT Green's functions can possibly be used in formal inversions for source parameters of an unknown moment tensor given displacement data. The next section addresses this.

The results also show that there is a frequency dependence in the performance of the corrective filter applied to the NCT in which higher frequency body waves are found to fall out of agreement

more quickly with increasing depth than the lower frequency waves. The high frequency surface wave agreement is also reduced for greater source depth showing mismatches in amplitude and some minor mismatches in phase.

4.0 RESULTS

4.1 Inversion with the Virtual Earthquake Approach

4.1.1 Introduction

Here we examine the inversion of synthetic displacement data for the moment tensor using the approximate GT, which is derived from the filtered NCT in the procedure described in Section 3.1. This is the inverse VEA problem, hereafter iVEA. We explore how the VEA approximations used in the conversion affect the final inverted moment tensor solution and solution uncertainty.

We propagate the error due to the VEA approximations into the final moment tensor, thereby investigating the theoretical bias of iVEA. In Section 3.1, we showed that when we converted a perfect NCT (synthetic unit-force response computed using FK-Integration for a surface focus) to the GT at seismogenic depth using fundamental mode surface wave eigenfunction spatial derivatives that the results were very good for surface waves and to a lesser degree for body waves (the VEA theory ignores body waves). This analysis thus showed that the resulting GT is an approximate representation. The question is to what degree do the ideal approximate GT affect the ability to correctly recover source parameters when applied in a moment tensor inversion scheme. The results of this test therefore represent a best case scenario for a iVEA application.

There are two issues that will affect the use of NCT in moment tensor inversion. The first is that while the theory allows for correcting for source depth there will be offsets of the seismic events of interest and the recording station used as the virtual source. To account for this error in practice, time adjustments will be allowed to align the NCT based GT with the earthquake waveform data. This can be done deductively based on time shifting records by a computed number of samples assuming traveltimes from a velocity model, or inductively by examining different values of time shifts to achieve maximum fit. The second issue is the amplitude of the NCT derived GT. While the relative amplitude information across a single NCT is preserved through the ambient noise processing, the absolute amplitudes are unknown. Thus we must interrelate all NCTs for the station pair paths used for source inversion. We do this by normalizing each NCT by the root-mean-squared amplitude of the synthetic 1-D frequency-wavenumber Green's tensor for the surface-surface path, whose amplitude is based on the moment of the seismic event of interest. In the synthetic examples shown below these steps were not required because the seismic source was generated directly below the epicentral station and the unit-force and dislocation-source Green’s functions computed with FK-integration have related unit amplitude.

4.1.2 Methodology

Inversion of (1) for the six elements of the symmetric full moment tensor is accomplished via a linear least-squares process (e.g. Jost and Herrmann, 1989; Pasyanos et al. 1996; Minson and Dreger, 2008). By convention, moment tensor inversion operates on the system of matrix equations wherein the *Mpq* is described in the Cartesian reference frame (NEU = XYZ). Here we provide

the trigonometric conversions between the conventional reference frame and the RTD reference frame used throughout the paper.

$$M_{TR} = M_{xx}\sin(\phi)\cos(\phi) - M_{xy}\cos^2(\phi) + M_{xy}\sin^2(\phi) - M_{yy}\sin(\phi)\cos(\phi) \quad 12a$$

$$M_{TD} = M_{xz}\sin(\phi) - M_{yz}\cos(\phi) \quad 12b$$

$$M_{RR} = M_{xx}\cos^2(\phi) + \left(M_{xy} + M_{yx}\right)\sin(\phi)\cos(\phi) + M_{yy}\sin^2(\phi) \quad 12c$$

$$M_{RD} = M_{xz}\cos(\phi) + M_{yz}\sin(\phi) \quad 12d$$

$$M_{DR} = M_{xz}\cos(\phi) + M_{yz}\sin(\phi) \quad 12e$$

$$M_{DD} = M_{zz} \quad 12f$$

The full set of equations for moment tensor inversion are here as an aside for future reference:

$$\begin{aligned}
\hat{u}_T(r,0,\omega) \approx & -ik_L sin(\phi)cos(\phi)\frac{L_1(z)}{L_1(0)}\hat{G}^A_{TT}M_{xx} \\
& + ik_L(cos^2(\phi) + sin^2(\phi))\frac{L_1(z)}{L_1(0)}\hat{G}^A_{TT}M_{xy} \\
& + ik_L sin(\phi)cos(\phi)\frac{L_1(z)}{L_1(0)}\hat{G}^A_{TT}M_{yy} \\
& - sin(\phi)\frac{1}{L_1(0)}\frac{\partial L_1(z)}{\partial z}\hat{G}^A_{TT}M_{xz} \\
& + cos(\phi)\frac{1}{L_1(0)}\frac{\partial L_1(z)}{\partial z}\hat{G}^A_{TT}M_{yz}
\end{aligned}$$

$$\begin{aligned}
\hat{u}_R(r,0,\omega) \approx & -ik_R cos^2(\phi)\frac{R_1(z)}{R_1(0)}\hat{G}^A_{RR}M_{xx} \\
& - 2ik_R sin(\phi)cos(\phi)\frac{R_1(z)}{R_1(0)}\hat{G}^A_{RR}M_{xy} \\
& - ik_R sin^2(\phi)\frac{R_1(z)}{R_1(0)}\hat{G}^A_{RR}M_{yy} \\
& - ik_R cos(\phi)M_{xz}\frac{R_2(z)}{R_2(0)}\hat{G}^A_{DR} - cos(\phi)M_{xz}\frac{1}{R_1(0)}\frac{\partial R_1(z)}{\partial z}\hat{G}^A_{RR} \\
& - ik_R sin(\phi)M_{yz}\frac{R_2(z)}{R_2(0)}\hat{G}^A_{DR} - sin(\phi)M_{yz}\frac{1}{R_1(0)}\frac{\partial R_1(z)}{\partial z}\hat{G}^A_{RR} \\
& - M_{zz}\frac{1}{R_2(0)}\frac{\partial R_2(z)}{\partial z}\hat{G}^A_{DR}
\end{aligned}$$

$$\begin{aligned}
\hat{u}_Z(r,0,\omega) \approx & -ik_R cos^2(\phi)\frac{R_1(z)}{R_1(0)}\hat{G}^A_{RD}M_{xx} \\
& - 2ik_R sin(\phi)cos(\phi)\frac{R_1(z)}{R_1(0)}\hat{G}^A_{RD}M_{xy} \\
& - ik_R sin^2(\phi)\frac{R_1(z)}{R_1(0)}\hat{G}^A_{RD}M_{yy} \\
& - ik_R cos(\phi)M_{xz}\frac{R_2(z)}{R_2(0)}\hat{G}^A_{DD} - cos(\phi)M_{xz}\frac{1}{R_1(0)}\frac{\partial R_1(z)}{\partial z}\hat{G}^A_{RD} \\
& - ik_R sin(\phi)M_{yz}\frac{R_2(z)}{R_2(0)}\hat{G}^A_{DD} - sin(\phi)M_{yz}\frac{1}{R_1(0)}\frac{\partial R_1(z)}{\partial z}\hat{G}^A_{RD} \\
& - M_{zz}\frac{1}{R_2(0)}\frac{\partial R_2(z)}{\partial z}\hat{G}^A_{DD}
\end{aligned}$$

To explore iVEA and understand how the VEA surface-wave approximation affects the inverted moment tensor solution, three-component displacement seismograms from a moment tensor source at a relatively deep depth (Z=3.1 km) were synthesized at four surface receivers of varying azimuth and regional distance (100-200 km) using the velocity model shown in Figure 2a and FK-integration method described above. In addition, synthetic NCTs between the four outer stations and a surface station located at the epicenter were generated by calculating displacement time histories for a surface-to-surface unit-force path. Application of iVEA inverts the exact seismic

data at the four outer stations with the filtered form of each NCT and yields a moment tensor solution, which can be evaluated against the known input moment tensor used to compute the exact seismograms. By varying the input moment tensor elements for a particular source type position we can assess the uncertainty introduced by the approximate Green's Tensor.

For inversion, we apply a 5% cosine taper to each end of the seismic record and the Green's function prior to applying a causal bandpass filter. We also apply inverse distance weighting to the Green's functions to account for energy radiation of the wavefield.

4.1.3 Results

Figures 5 and 6 show the ideal reference pure double-couple source case at 3.1 km for source inversion with low (0.02-0.1 Hz) and high frequency (0.1-0.5 Hz) filters and the present station geometry in which the same exact GT is used to compute the synthetic data and to invert it. We use these solutions as a baseline to evaluate the iVEA results. Note how the moment tensor inversion retrieves the input moment tensor solution exactly for the two passbands shown, but the source-type inversion recovers an equal contour of fit in terms of variance reduction that spreads in the isotropic axis approximately +/-25%. The spread along the deviatoric line is much greater (+/-50%). The same is true of a shallow solution, see Nayak and Dreger, 2015 for more details on the cause of this uncertainty, which is related to the long-period nature of the data.

Figures 7 and 8 show the iVEA results for a deep source depth (Z=3.1 km) with a pure-double-couple input, for the 0.02 to 0.1 Hz and 0.1 to 0.5 Hz passbands, respectively. We find that the VEA approximations for this source type (normal event) introduce a small error into the GT (e.g. Figure 4), which degrades the model fit. Despite this error the solution mechanism is unchanged. At low frequencies, the best fit moment tensor solution is reduced from 100%VR to 95%VR, but the uncertainty in the vertical isotropic axis as shown by the source-type inversion is not significant. Comparing inverted and model data indicates that the majority of the misfit is due to the body wave term, specifically in Radial and Vertical components. At higher frequencies, fit degrades to 88% and the body wave misfit is more apparent as expected from the results of Section 3.1. The source-type uncertainty is similar to what was observed in Ford et al. (2010) and Nayak and Dreger (2015) for real data inversions.

Figures 9 and 10 show the iVEA results for a shallow source depth (Z=0.8 km) with a pure double-couple input, for the 0.02 to 0.1 Hz and 0.1 to 0.5 Hz passbands, respectively. We find that the VEA approximation error depends on depth as expected from the VEA equations; model fit is slightly better at 0.8 km (VR=98%) than at 3.1 km (VR=95%). The solution mechanism is again unchanged and uncertainty introduced by iVEA is again insignificant based on source-type inversion. The majority of the misfit appears to be due to the body wave term, specifically in Radial and Vertical components which is stronger at higher frequencies. Fit degrades to 88.5% in the higher frequency case.

Figures 11 and 12 explore the iVEA for the present geometry and a non-double couple case of a positive 70% isotropic seismic source at deep (Z=3.1 km) and shallow source depth (Z=0.8 km), both for the 0.1 to 0.5 Hz passband. Because the VEA approximation error depends on depth there is a larger uncertainty in the solution (VR=85% and larger deviation from input in Hudson space)

at 3.1 km depth. At 0.8 km the fit improves to 88.5% and the solution on the Hudson diagram is more accurate.

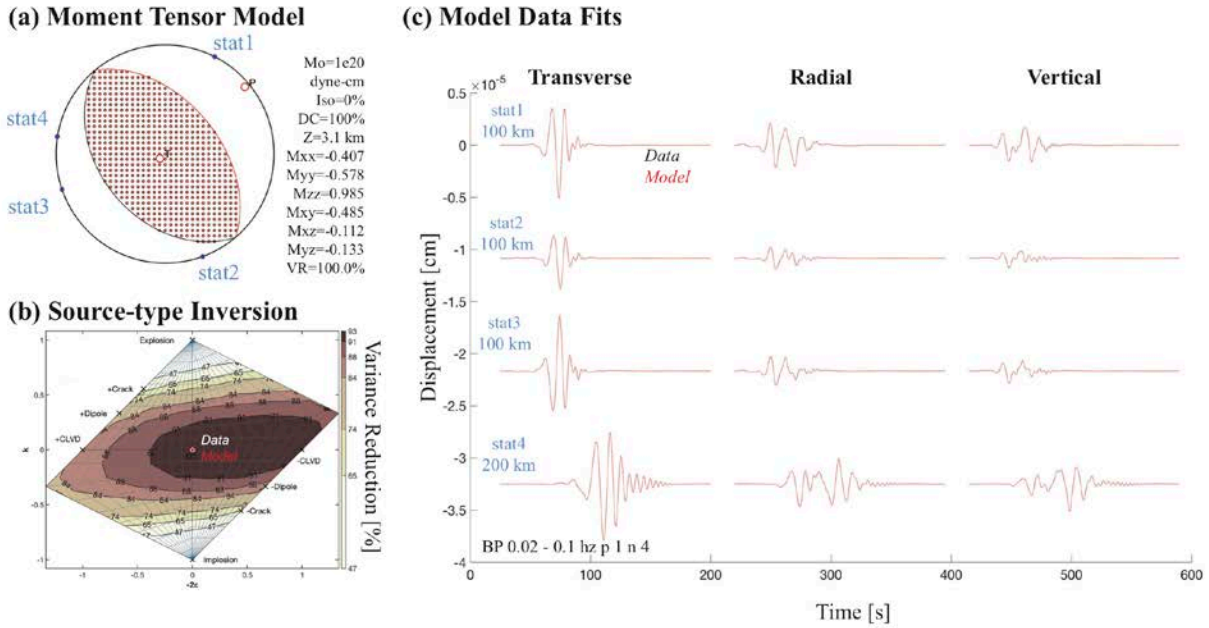

Figure 5. Results for a synthetic deep (z=3.1 km) pure double-couple earthquake recorded by 4 surface stations (d=100-200 km) with LF filter (BP 0.02 0.1 p 1 n 4). *This is the low freq. ideal or reference case where GFs used to compute and invert data are the same (VR = 100%). (a) Lower hemisphere projection of solution (red) superimposed on the input tensor used to compute data (black). (b) Source-type inversion in the Hudson space. Note how the uncertainty in any model solution with VR>95% extends to +/-25% isotropic. (c) Data (black) and model data fits (red).*

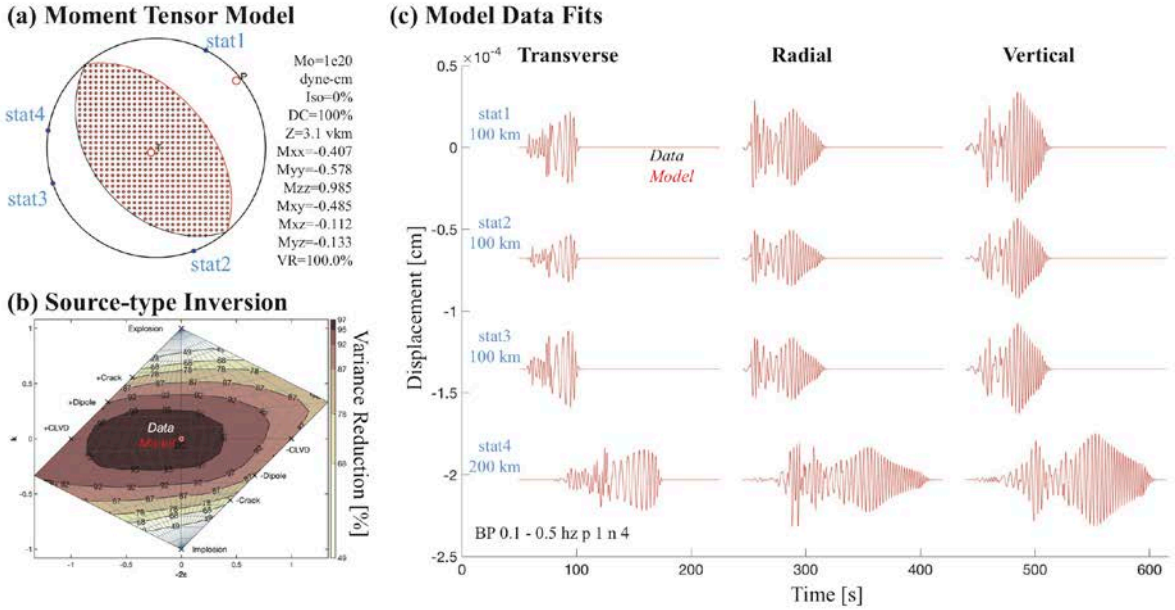

Figure 6. Results for a synthetic deep (z=3.1 km) pure double-couple earthquake recorded by 4 surface stations (d=100-200 km) with HF filter (BP 0.1 0.5 p 1 n 4). *This is the high freq. ideal or reference case where GFs used to compute and invert data are the same (VR = 100%). See Figure 5 for individual axis captions. Difference between Figure 5 and 6 is the filter passband.*

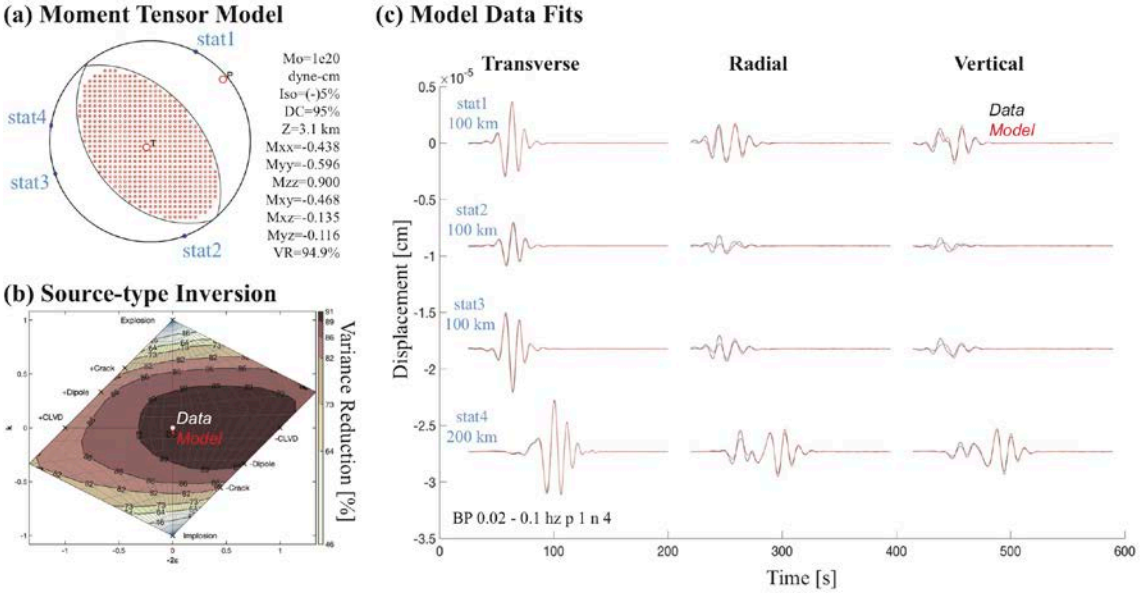

Figure 7. Results for a synthetic deep (z=3.1 km) pure double-couple earthquake recorded by 4 surface stations (d=100-200 km) with LF filter (BP 0.02 0.1 p 1 n 4). *This is a synthetic iVEA test case where GFs used to compute data are ideal (buried FKI) but GFs used to invert data are converted surface synthetic NCTs. See Figure 5 for individual axis captions.*

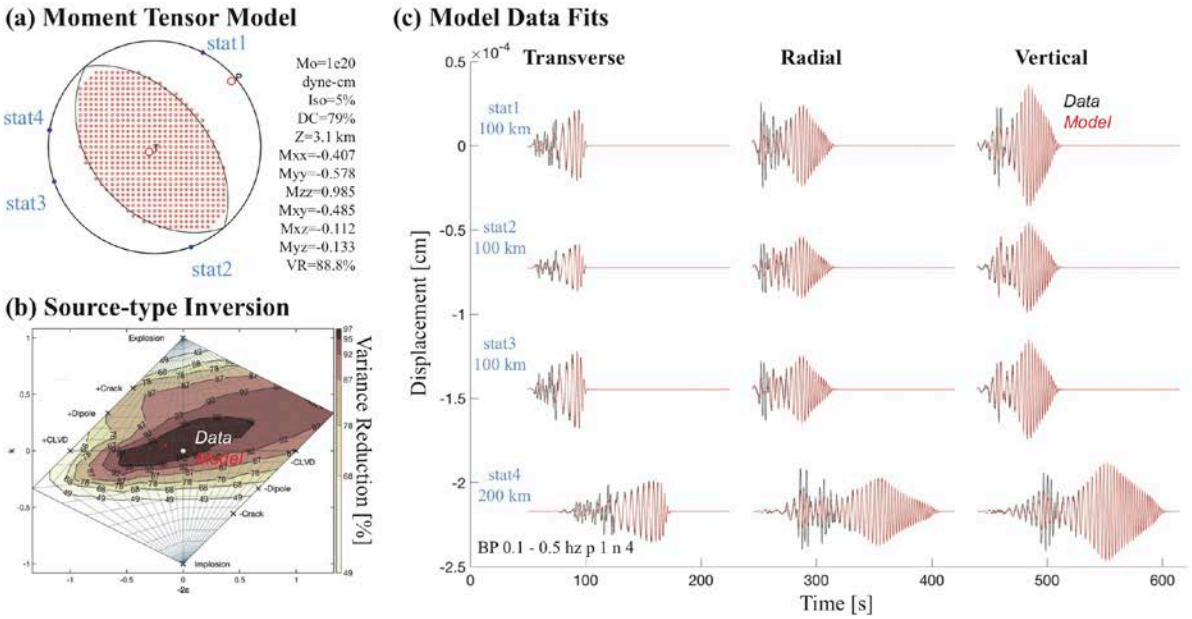

Figure 8. Results for a synthetic deep (z=3.1 km) pure double-couple earthquake recorded by 4 surface stations (d=100-200 km) with HF filter (BP 0.1 0.5 p 1 n 4). *This is a synthetic iVEA test case where GFs used to compute data are ideal (buried FKI) but GFs used to invert data are converted surface synthetic NCTs. See Figure 5 for individual axis captions. Difference between Figure 7 and 8 is the filter passband.*

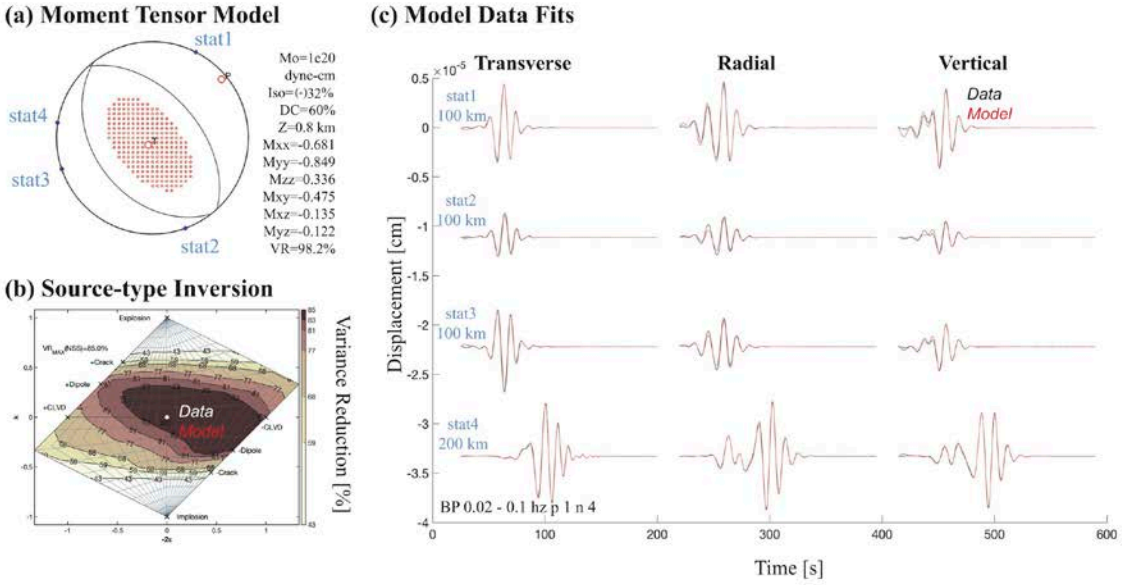

Figure 9. Results for a synthetic shallow (z=0.8 km) pure double-couple earthquake recorded by 4 surface stations (d=100-200 km) with filter BP 0.02 0.1 p 1 n 4. *This is a synthetic iVEA test case where ideal GFs are used to compute data but converted surface synthetic NCTs are used as approximate GFs to invert data. See Figure 5 for individual axis captions Difference between Figure 7 and 9 is source depth.*

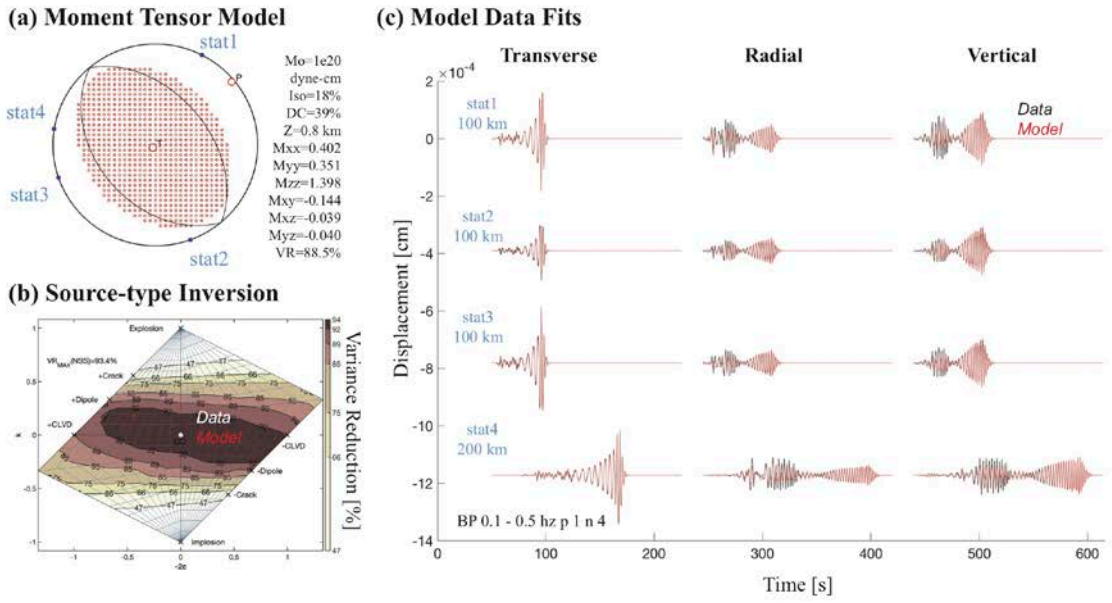

Figure 10. Results for a synthetic shallow (z=0.8 km) double-couple case recorded by 4 surface stations (d=100-200 km) with filter BP 0.1 0.5 p 1 n 4. *This is a synthetic iVEA test case where ideal GFs are used to compute data but converted surface synthetic NCTs are used as approximate GFs to invert data. See Figure 5 for individual axis captions. Difference between Figure 9 and 10 is filter passband.*

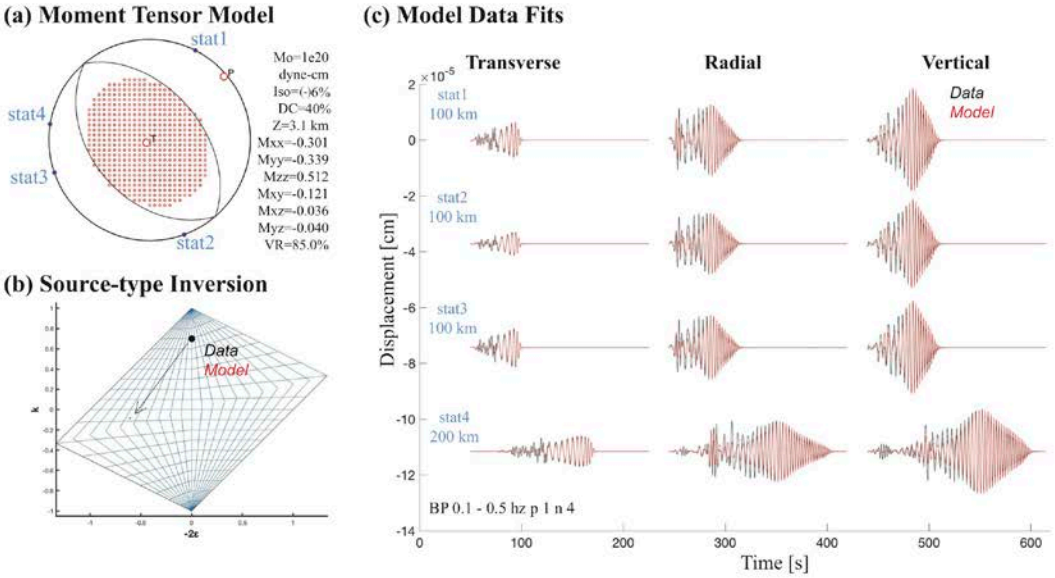

Figure 11. Results for a synthetic deep (z=3.1 km) non-double-couple case with 70% isotropic and 30% double-couple recorded by 4 surface stations (d=100-200 km) with filter BP 0.1-0.5 Hz p 1 n 4. *This is a synthetic iVEA test case where GFs used to compute data are ideal (buried FKI) but GFs used to invert data are converted surface synthetic NCTs. See Figure 5 for individual axis captions. The difference between Figure 7 and 11 is the isotropic source component.*

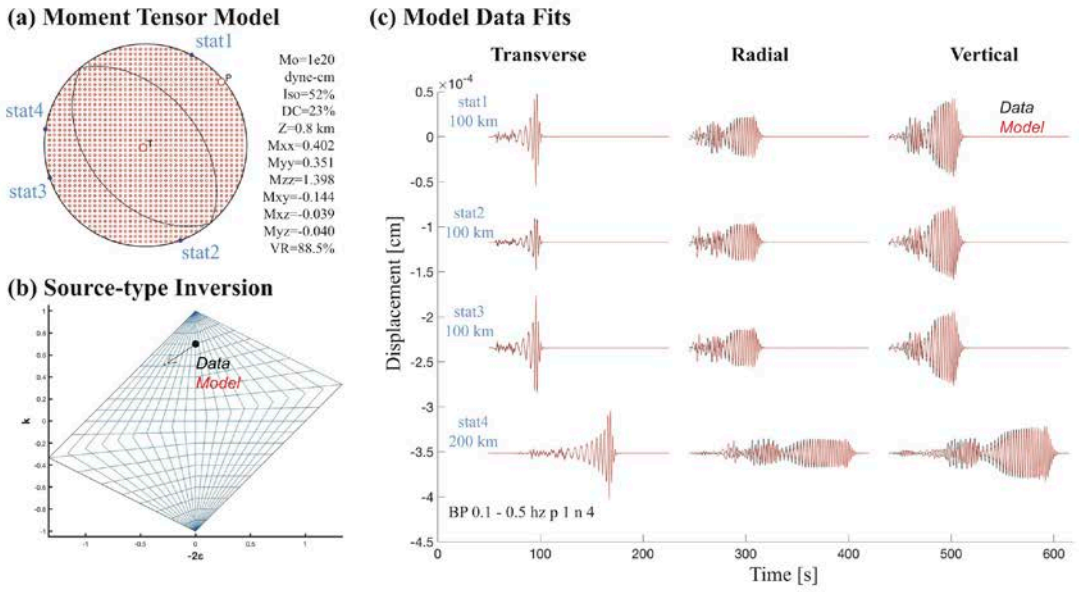

Figure 12. Results for a synthetic shallow (z=0.8 km), 70% isotropic, non-double-couple case with 70% isotropic and 30% double-couple recorded by 4 surface stations (d=100-200 km) with filter BP 0.1-0.5 Hz p 1 n 4. *This is a synthetic iVEA test case where GFs used to compute data are ideal (buried FKI) but GFs used to invert data are converted surface synthetic NCTs. See Figure 5 for individual axis captions. The difference between Figure 11 and 12 is the source depth; note how the retrieved source type model is more accurate for a shallower depth.*

Summarizing these results for the pure-double couple cases (Figures 7-10) it is found that errors in recovered iVEA solutions increase for larger depths due to the greater correction to map from surface-focus to depth-focus. It is also observed that errors increase in the higher frequency and narrower passband (0.1 to 0.5 Hz) compared to the lower frequency passband (0.02 to 0.1). This is expected as the wider passband carries more information and is less subject to errors caused by changes in phase due to the depth and mechanism correction of the NCT. Overall the extent of the best fitting region in the source-type inversion results is comparable to what has been observed in real earthquakes (e.g. Ford et al., 2010; Nayak and Dreger, 2015) indicating that the uncertainties due to NCT corrective filtering are not appreciably higher than what is expected due to the low-frequency nature of the waveforms used in the inversion, or due to other causes like network topology, velocity model, and noise in the data. For the non-double-couple cases (70% isotropic, 30% double-couple), Figures 11-12, the results show significant error in the source-type for the deeper source (3.1 km), whereas for the shallow source (0.8 km) the non-double-couple character of the solution is well recovered, although there is a significant CLVD component that is introduced (Figure 12). The results are found to appreciably improve when the wider low-frequency passband (0.02 to 0.1 Hz) is employed (Figure 13).

For the 0.02 to 0.1 Hz passband we evaluated the solution uncertainty of 25 iVEA realizations for a particular input source-type to understand the range of possible solutions. In Figure 13 the iVEA solutions are plotted as an error ellipse around the input mechanism on the Hudson diagram. We find that iVEA uncertainty depends on source type. In each case, there is at most a +/-10% isotropic component introduced, meaning the uncertainty in the isotropic axis is minor when compared with the average uncertainty in regional time domain moment tensor inversion. This is a positive result for source-type discrimination applications of possible explosive events. However, for a double-

couple moment tensor of intermediate isotropic source-type, we find that the error in the retrieved moment tensor along the CLVD axis is approximately +/-40%. This error increases to as large as 60-70% when the input moment tensor has a large CLVD component. The magnitude of these errors are similar to what has been found from bootstrapping residuals, Jackknife testing, and NSS/Source-type-inversion (Ford et al., 2009a; Ford et al., 2010, Nayak and Dreger, 2015, Boyd et al., 2015, Dreger, 2018).

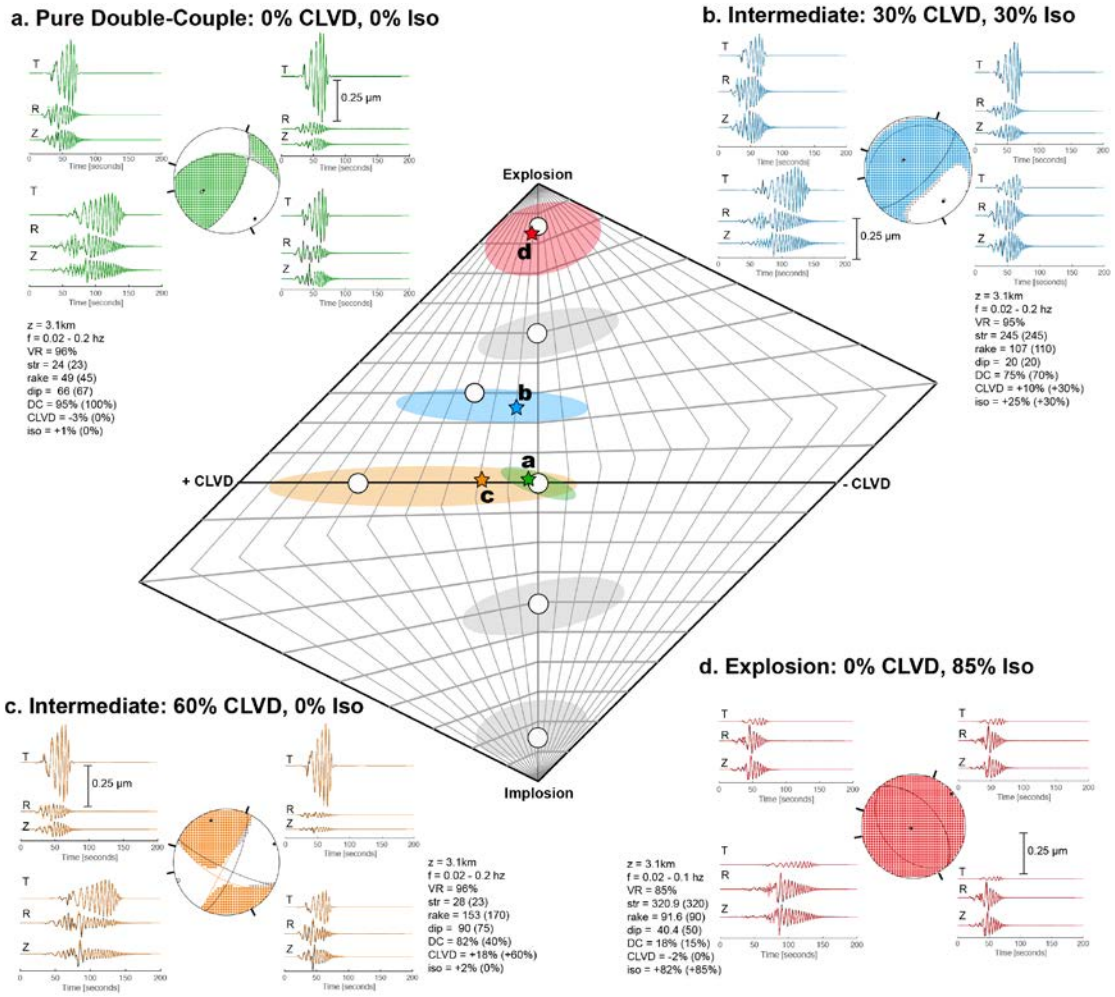

Figure 13. Results of iVEA synthetic testing show how the VEA Green's tensor surface wave approximations introduce a source-type dependent error in the Hudson source-type space, which is bounded along the isotropic axis by approximately +/- 5-10%. *Examples highlighted in color show 1-D FKI synthetic station data (TRZ, BP=0.02-0.2 Hz) [black waveforms] calculated using a chosen moment tensor at 3.1 km depth [black MT], the 4-station inverted moment tensor solution [color MT], and the solution data fits [color waveforms]: a) Pure DC; b) Intermediate (30% +CLVD, 30% isotropic); c) Intermediate (60% +CLVD); d) Explosion (85\% isotropic). The body wave arrivals generate the largest misfit. Details of input and solution models are given in the sidebar for each example. Tickmarks around the MT diagram's perimeter indicate station azimuth. Station-epicenter offset is 100 km, except for the station to the lower left (261°) which is 200 km away.*

4.1.4 Discussion and Conclusions

The no-noise synthetic inversions using the corrected/filtered NCT reveal three important results.

First the bias in isotropic moment estimates is small when compared with the inherent uncertainty of moment tensor inversion. In real numbers, moment tensor solutions with exact Green's functions can range +/-15% along the isotropic axis, and the uncertainty is no worse in this way when the corrected NCT is used instead. This is a positive result for the nuclear source-type discrimination application.

A second observation is that there are significant non-double-couple uncertainties introduced by the corrected/filtered NCT, that depend on the earthquake mechanism. These errors are of the same magnitude as found due to noise in regional distance data, sparse network coverage and imperfect velocity structures from residual boot-strap, Jackknife and NSS/Source-Type-Inversion analyses (e.g. Ford et al., 2009a; Ford et al., 2010, Nayak and Dreger, 2015, Boyd et al., 2015 and Dreger, 2018).

Third, the results comparing a source depth of burial of 800m vs 3100m demonstrate that the VEA equation approximations are best for shallow focus studies, which is a positive attribute for possible source-type discrimination of shallowly buried explosions.

It can also be said that errors in narrow and/or high-frequency passbands (0.1 to 0.5 Hz) are larger and as shown for the deep source case significantly mis-identify the source-type. It appears that for the shallow case the error due to the narrow high-frequency passband is not as large owing to the lesser degree of correction applied to the NCT.

4.2. Application of iVEA at The Geysers Geothermal Field

4.2.1 Introduction

Our aim in this section is to test iVEA using real data for seismic events that have already been modeled using a classical time-domain moment tensor approach with 1-D Green's functions over short path lengths (<5 km), thereby evaluating both the methods for the estimation of NCT from ambient noise and the inversion for the full moment tensor.

The Geysers geothermal field in Northern California is among the world's largest geothermal energy production systems with a total capacity of 768 MW, and is well-known to the seismological community as a site of induced seismicity related to fluid-injection (Majer and McEvilly, 1979, Oppenheimer 1986, Majer and Peterson, 2007). As such, The Geysers has been the site of decades of geophysical characterization studies, including well-logging, body-wave travel-time tomography, and reservoir modeling. Although knowledge of how seismic waves propagate through this complex structure is still imperfect (Nayak et al., 2017), there have been recent and thorough efforts to characterize small magnitude seismic and microseismic source characteristics with specific attention to non-double-couple moment tensors (Guilhem et al., 2014; Boyd et al., 2015; Johnson et al., 2017; Vavryčuk, 2018).

To estimate the ambient noise correlation tensor (NCT) used in the iVEA we use continuous recordings of ambient noise from The Geysers (see Section 3.3.2. for details on the data). Simultaneous recordings of ambient noise on two seismic sensor components can be cross-correlated in a workflow to extract information about seismic waves propagating between the two sensors, as if one was a virtual source of seismic energy (Campillo and Paul, 2003; Sneider, 2004; Curtis et al., 2006; Lin et al., 2008; Hadziioannou et al., 2009; Wapenaar et al., 2010). This form of seismology, called ambient noise seismology or seismic interferometry, is now routinely applied as a technique to extract surface wave dispersion curves and invert for phase velocity or group velocity information about the Earth, as well as model body wave propagation (Nakata et al., 2014). Rigorous treatment of the noise data processing workflow required to robustly retrieve the signal from the noise is the subject of only a limited number of papers (Bensen et al, 2007; Seats et al., 2012; Viens et al., 2017). The results suggest that the actual procedure used needs to be evaluated for each specific application and region due to variations in the noise sources. Section 3.3.3 begins with a description of the procedure we applied and the reasons behind our choices. We test iVEA using NCT obtained using two different interferometric approaches.

4.2.2 Data

To supplement the short-period seismic network in the vicinity of The Geysers, CA, broadband seismic stations were installed in 2012 by Dr. Roland Gritto. Stations were located in and around The Geysers Geothermal Field extending out to approximately 60 km.

Each station consisted of a 3-component surface sensor (Guralp CMG-3ESP or Trillium Compact), a Ref-Tek digitizer, and power supply, recorded continuously with very few gaps for a period of about 1 year. Data were provided as 30 minute duration time series files in miniSEED format at a native sampling rate of 200 Hz. The broadband stations have a flat instrument response function from 120 s to 50 Hz, which was removed before data processing.

We chose to evaluate a seismic event whose epicenter was within 1 km of station AL4 located in the northwest region of The Geysers using 7 stations that ranged from 2 km to 54 km away from AL4, because these paths balance high signal-to-noise ratio of the energy of the Mw2.87 seismic event with the coherency of ambient noise propagation in the ocean microseism band (0.05 – 0.5 Hz) which we are interested in for modeling the earthquake source properties (see Figure 14). This choice is important and will be discussed in greater detail in the discussion (Section 3.3.4).

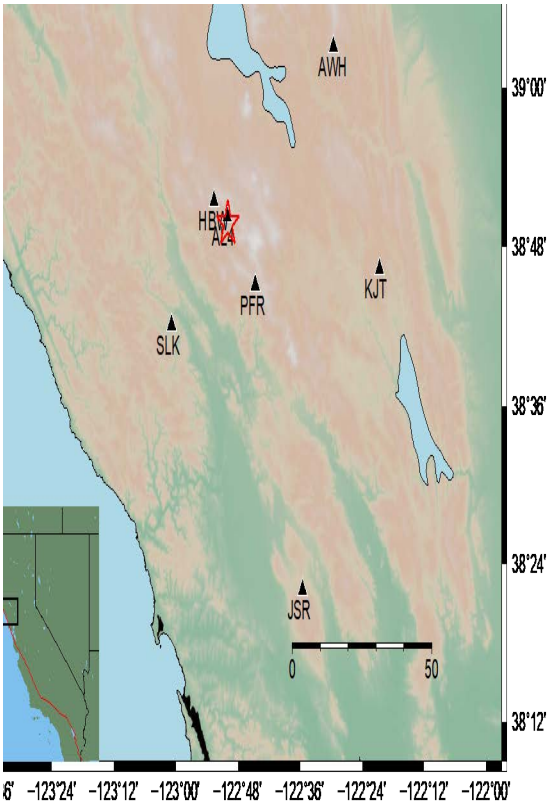

Figure 14. Map of The Geysers Geothermal Field, CA indicating broadband seismometer stations (black triangles) and the Mw2.87 earthquake (red star). *Note that AL4 is located nearest the epicenter.*

4.2.3 Methodology:

Noise Correlation Tensor estimation: Workflow Design

We aim to use iVEA to invert seismic records from the Mw2.87 Feb-21-2012 earthquake. Because this seismic event occurred at a hypocentral depth of 1.5 km below AL4, we compute NCTs between AL4 and stations that recorded the seismic event to form a local network of good coverage in terms of azimuth and take-off angle. We next compute NCTs between station AL4 located inside The Geysers and 7 surrounding stations (HBW, PFR, SLK, KJT, AWH, CSH, JSR). We broadly follow workflow recipes from the ambient noise seismology literature with deviations that were based on our experience of what worked from experimenting with these data. The steps to compute a single station pair NCT are as follows:

- Instrument Response Removal
- Rotate from NEZ → RTD
- Divide continuous data into 30 minute windows
- Cosine Taper (2%, Hanning window, both ends)

- Linear detrend
- Bandpass filter (0.1-0.5 Hz, p 1 n 4)
- Screen and remove impulsive earthquakes and other spikes
- NCT computation for 1 window (Cross-correlation, Coherency, Deconvolution)
- Linear stack of all windows
- Average causal (positive lag-times) and acausal (negative lag-times) NCT data

We design our pre-processing and cross-correlation workflow using template workflows published by Bensen et al. (2007), Seats et al. (2012) and Lin et al. (2013). Data processing involves first removing the instrument response, then rotating from North-East-Vertical to Transverse-Radial-Vertical based on the known interstation back azimuth with station AL4. Then individual component records were pre-processed according to the Welch's method using non-overlapping windows of 30-minute duration (Seats et al., 2012). For each 30-minute window, data were tapered on both ends using a Hanning window with a 2% taper length, detrended using the fit of a linear trend, and filtered in the dominant seismic band from 0.1 - 0.5 Hz using a causal, forth-order bandpass filter.

The next step in the ambient noise workflow is a screening process that is designed to remove local, regional, and teleseismic seismic event arrivals, as well as any spurious spikes that bias the final NCT estimate. We developed an automatic procedure to select the problematic windows where if the energy of any one sample in the window exceeds a threshold of 10 times the standard deviation of the energy of all of the window's samples it is discarded in the stack. In Figure 15, the 30 m duration biased windows for a 24-hour period are labeled red and the windows that passed this threshold are labeled green.

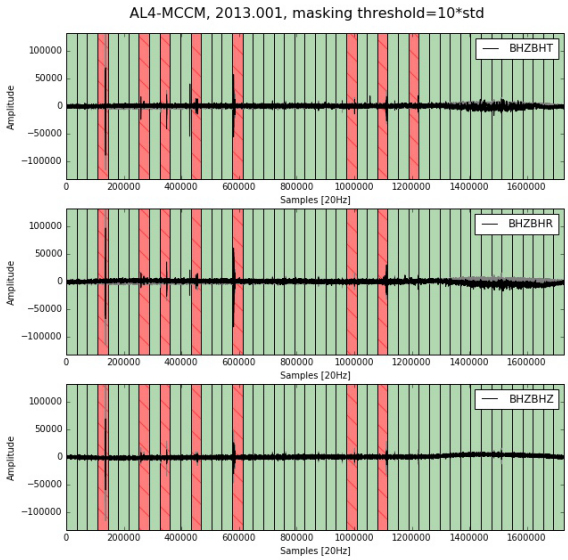

Figure 15. Three-component example for an example AL4-station showing the selection and windowing process used in the noise correlation workflow. *Simultaneous records of 30-minutes of data are filtered and processed together. Impulsive earthquake arrivals are removed based on a threshold of the window energy.*

Following data processing, we compute the 9 component NCT for each 30 minute window using the 3 component data from each station. This computation has traditionally been casually referred to as cross-correlation, which is defined as time-domain convolution. In most cases, studies involving cross-correlation have also involved spectral division of the resulting quantity's spectra by the energy of the virtual source station's spectra (also called deconvolution) or the product of the energy of the virtual source spectra and virtual receiver spectra (also called coherency):

$$C_{ij}(x_r, x_s, t) = f^{-1}\left(\frac{\hat{v}_i(x_r,\omega) * \hat{v}_j(x_s,\omega)}{\{|\hat{v}_j(x_s,\omega)|\}\{|\hat{v}_i(x_r,\omega)|\}}\right) \quad 13a$$

$$D_{ij}(x_r, x_s, t) = f^{-1}\left(\frac{\hat{v}_i(x_r,\omega) * \hat{v}_j(x_s,\omega)}{\{|\hat{v}_j(x_s,\omega)|\}^2}\right) \quad 13b$$

These spectral divisions (also so-called spectral normalization) usually are only successful when implemented with a water-level type smoothing operator to avoid the 'divide-by-zero' condition where the spectra have near-zero energy. Estimates of noise correlation were shown by Viens et al., 2017 to retrieve useful Green's tensor estimates and preserve relative amplitude information through inclusion of spectral information. To simplify vocabulary, we will call these methods coherency and deconvolution. In our study, the coherency and deconvolution NCTs were computed using a ten-point running average. We will compare these two estimates in the moment tensor estimation with iVEA.

We then average the NCT estimates for each window by computing the mean of all selected windows over a six-month period between January - June 2012. Six months was chosen as a sufficiently converged NCT because the form of the functions in the time domain did not appear to change. Finally, we average the causal and acausal sides of the resulting functions.

Noise Correlation Tensor estimation: Convergence and Accuracy of NCT

An underlying concept of the empirical ambient noise method generally, and iVEA specifically, is that the resulting NCT retrieved for any path contains complex wave propagation information that would otherwise be too laborious to construct. For example, wave propagation through a 50 km x 50 km x 5 km volume in a finite difference mesh designed to model f ~ 0.5 Hz (assuming 1000 m / s average seismic velocity and 10 nodes per wavelength) would require 200 m node spacing and over 1.8e6 nodes in the mesh. The computational demands aside, such calculations require models of velocity structure at scales that are not possible to constrain. That is not to say that such calculations are warrantless, they most certainly can improve wave propagation and source parameter recovery with relatively simple 3D model (e.g. Covellone and Savage, 2012). But, the required scale for accurate simulation of 0.5 Hz waves points to the need to also explore empirical means of constraining 3D wave propagation influences. However ambient noise correlation approaches are also difficult to verify and suffer from known source field limitations when, for example, the source field cannot be assumed to be uniform in azimuth and power (Wapenaar et al., 2010). This is why we choose to refer to the result of the ambient noise procedure as a noise correlation function and not a 3-D Green's Function. Methods are being pursued that seek to take into account the source field biases, but this is still an open topic of research (Sager et al., 2018).

Figure 16 shows the resulting TT components of two NCTs as functions of increasing stack count, or incremental window. This demonstrates that the signal-to-noise ratio of the major phase arrivals stack in over time.

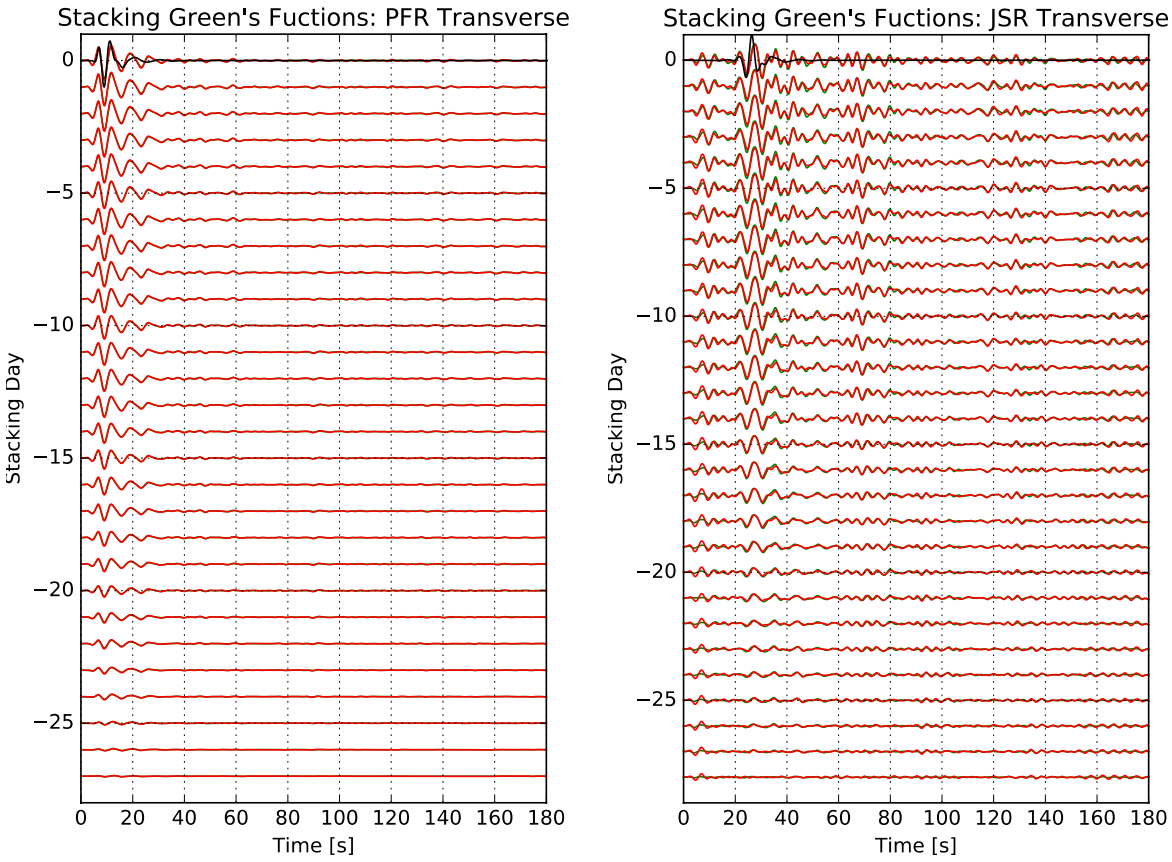

Figure 16. Transverse-transverse NCT components between (left) AL4 and PFR, (right) AL4 and JSR showing emergence of a fundamental mode Love wave arrival visible after less than 30 days (BP 0.1 – 0.5 Hz). *The noise correlations are shown in (red) with the 1-D synthetic frequency-wavenumber integrated TT component (black).*

In evaluating the proposed NCT workflow at The Geysers we find that convergence occurs after several months when using Welch's method of windowing and sampling with a 30 minute duration as recommended by Seats et al., 2012. Figure 17 shows the convergence of the 9 tensor elements for the AL4-JSR station pair, where after 100 days the rate at which the waveforms change with additional daily stacks begins to decrease, and by 120 days the change in prior window correlation for subsequent statics has for the most part leveled off. We utilized 180 day stacks in our analysis. Figures 18 – 20 show 1-D synthetics with the converged 180 day NCTs for the TT, RR, DD components for each of the station paths used at The Geysers in the BP 0.2-0.4 Hz passband. For some of the station pairs there is good correspondence between the NCT and the 1D synthetics, which helps to provide confidence that the procedure to estimate the NCT is working, as well as indicating for those particular paths the velocity model used to estimate the

synthetics is appropriate for the path. This suggests too that the model would be suitable for use in the filtering process of the NCT to estimate the GT used in the inversion. For other paths there are significant differences between the 1D synthetics and the NCT which provides evidence of complex path effects.

We note that assessing NCT convergence is difficult, beyond the typical *ad hoc* approach of evaluating NCT stability with increasing stack. To additionally evaluate the accuracy of the converged NCTs we compare several waveform features of the 1-D synthetic GTs and the NCTs, such as first arrival times, coda envelopes, and the balance of energy across the tensor (i.e., was the dominant energy of the NCT located in the TT, RR, DD, DR, RD components, as expected from a 1-D theory of wave propagation). If the ambient noise source field is well-behaved then these waveform features should be similar. For example, equipartitioning of the noise source field will lead to a canceling of noise source energy that arrives at t=0, and therefore the NCT, like the 1-D GT, should have approximately the same first arrival time with a low pre-event noise level. Additional energy in the NCT waveforms may be due to 3-D wave propagation effects that are not included in the 1-D velocity model.

In Figure 21 the final complete NCT for station pair AL4-HBW is compared with the 1D synthetics. There is general agreement with the 1D synthetics indicating that for this path on average it is close to the velocity model that was used to estimate the synthetics. However, there are also notable differences particularly for component pairs that include a vertical component. This may indicate some effects of 3D wave propagation. The off diagonal terms of the NCT, TR, RT, TZ, and ZT show coherent arrivals that indicate some 3D wave propagation along this path. Finally, both the coherency and deconvolution NCT are compared, and it is seen that they are similar to each other, more so than they are with the 1D synthetics, but they are not identical. This illustrates the uncertainty in the NCT estimates that results from the specifics of how the NCT are determined. This observation is important because if these functions are used for ground motion simulation or for source inversion there will be errors and uncertainty in the source parameters or ground motions due to the uncertainty in the derived NCT functions. With the stability results and the comparison with 1D synthetics being largely positive we assume that the ambient noise source field assumptions are valid in this scenario after 180 days (6 months) of stacking, and move on to use them in iVEA.

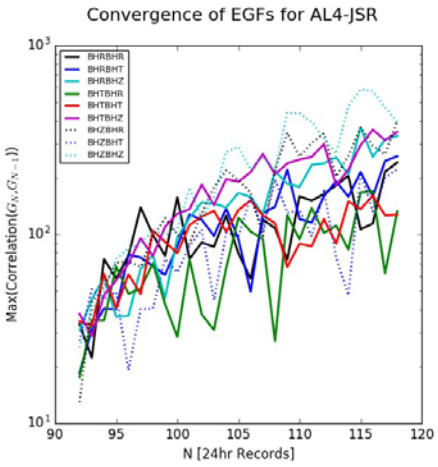

Figure 17. Plot of the correlation between the NCT of each additional window for the AL4-JSR NCT over the first 4 months shows a convergence for all components.

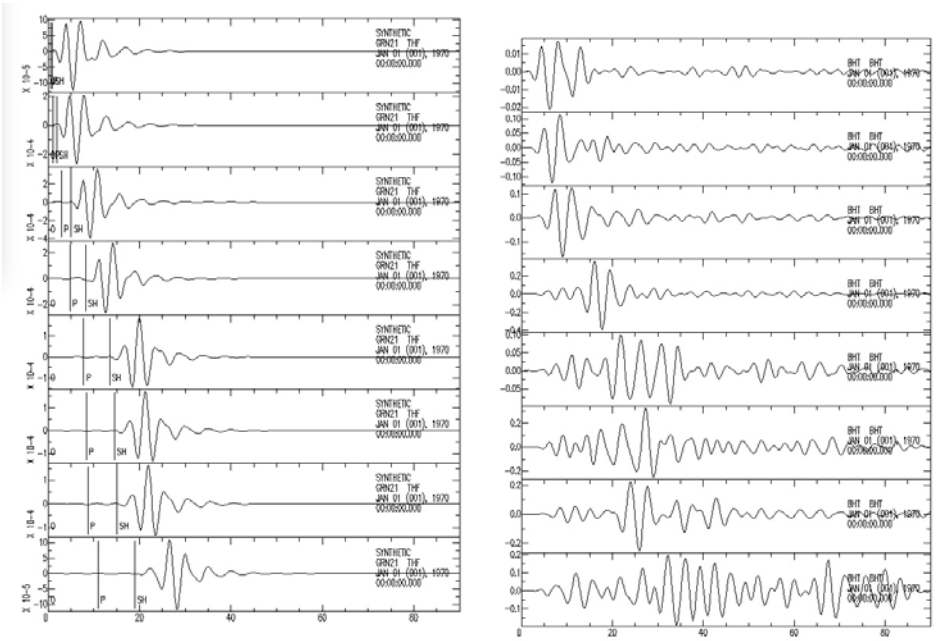

Figure 18. Transverse-transverse synthetic Green's functions for REF1.0 (left) and (right) converted TT coherency estimates (180 day stacking) between AL4 and the same stations shown in Figure 14 (MCL, HBW, PFR, SLK, KJT, AWH, CSH, JSR; from top to bottom). BP 0.2 – 0.4 Hz p 1 n 4.

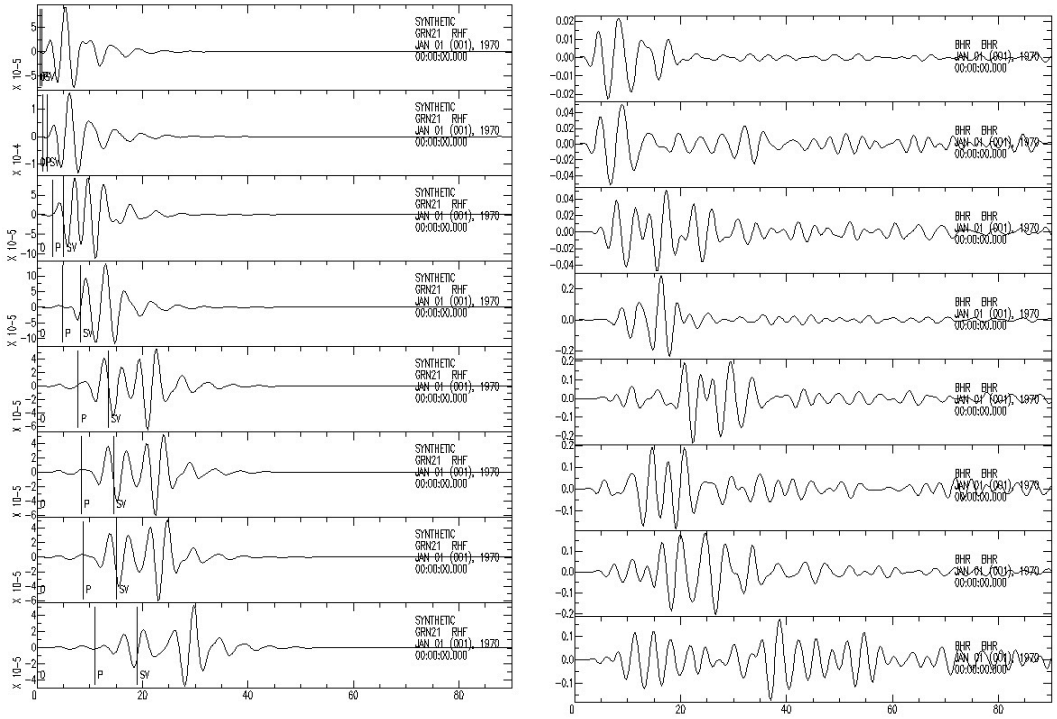

Figure 19. Radial-radial synthetic Green's functions for REF1.0 (left) and (right) converted RR coherency estimates (180 day stacking) between AL4 and the same stations shown in Figure 14 (MCL, HBW, PFR, SLK, KJT, AWH, CSH, JSR; from top to bottom). BP 0.2 – 0.4 Hz p 1 n 4.

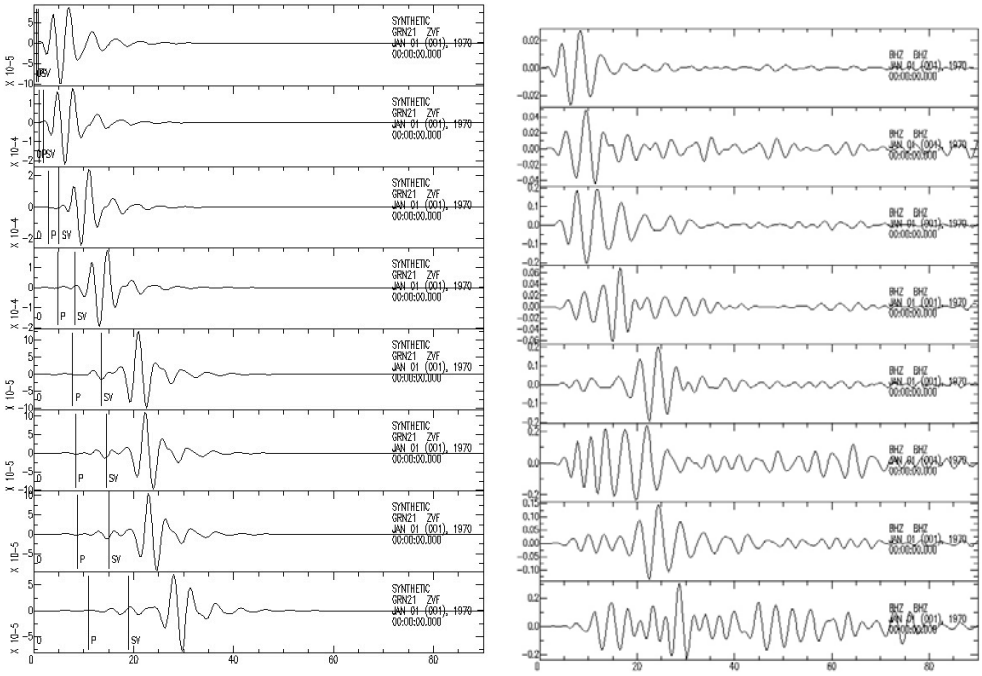

Figure 20. Vertical-vertical synthetic Green's functions for REF1.0 (left) and (right) converted DD coherency estimates (180 day stacking) between AL4 and the same stations shown in Figure 14 (MCL, HBW, PFR, SLK, KJT, AWH, CSH, JSR; from top to bottom). BP 0.2 – 0.4 Hz p 1 n 4.

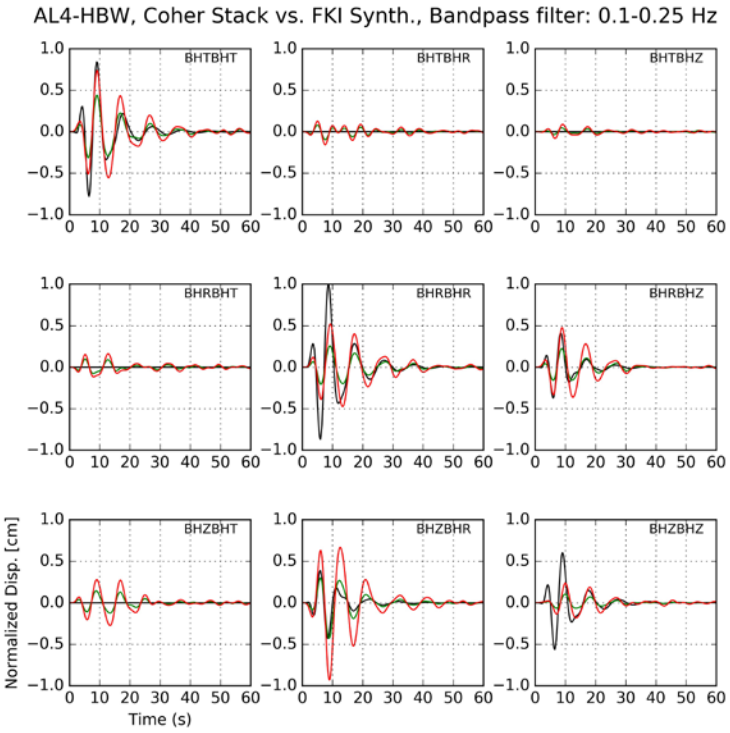

Figure 21. Final full noise correlation tensor estimates (red=Coherency; green=Deconvolution) plotted with 1D FKI synthetics (black) for station pair AL4 and HBW. BP 0.1 – 0.25 Hz.

Application of iVEA to an Earthquake

On Feb-21-2012, a small Mw2.87 earthquake occurred at 1.5 km depth in the northwest Geysers. Boyd et al., 2018 applied the inversion approach of Guilhem et al., 2014 to estimate the full moment tensor solution for this event based on the seismic waveforms (f=0.25 - 1 Hz) and first motion polarities recorded on stations located within 5 km of the epicenter, and we use this solution as control in evaluating the iVEA approach.

We apply the methodology of Section 3.1.2 to convert the unit-force surface-surface NCTs computed above to the earthquake depth, approximate dislocation source GFs used in moment tensor inversion. Prior to inversion, we take into account the differences between NCT amplitudes for the specific paths, because the NCTs have differences in relative amplitudes amongst each other (typically normalized to 1 within the tensor) that must be interrelated for the purposes of inversion. We choose to scale each ambient NCT by the mean RMS amplitude of the station pair 1-D unit-force Green's tensor computed using Green's functions for velocity model REF 1.0. A different approach would be to develop a network average station pair NCT estimate, but this is left for future work.

4.2.4 Results

We first perform a test inversion using synthetic NCT and the moment tensor provided by Boyd et al. (2018). Synthetic data were computed using dislocation source Green's functions, whereas the Green's functions used in the inversion where constructed by applying the approximate corrections in section 3.1.2 to surface focus unit-force Green's functions. This test shows that with the synthetic NCT it is possible to obtain a solution close to the input solution (Figure 22). The differences between the input and recovered moment tensors is indicative of the errors introduced by the approximate nature of correcting the NCT for use in iVEA as discussed in section 3.2.

The next test was to use theoretical Green's functions for an appropriate velocity model to invert the data in the 0.1 to 0.5 Hz passband (Figure 23). The results of this test show that it is not possible to use the data in the higher frequency passband at these distances to recover the moment tensor using the 1D velocity model Green's functions. Recall that the mechanism obtained by Boyd et al. (2018) utilized much closer stations where the assumed 1D velocity model was appropriate for the passband that was used. In the case shown in Figure 23 the data for the earthquake is significantly more complex than the 1D Green's functions.

Synthetic Data; Synthetic 1-D GFs

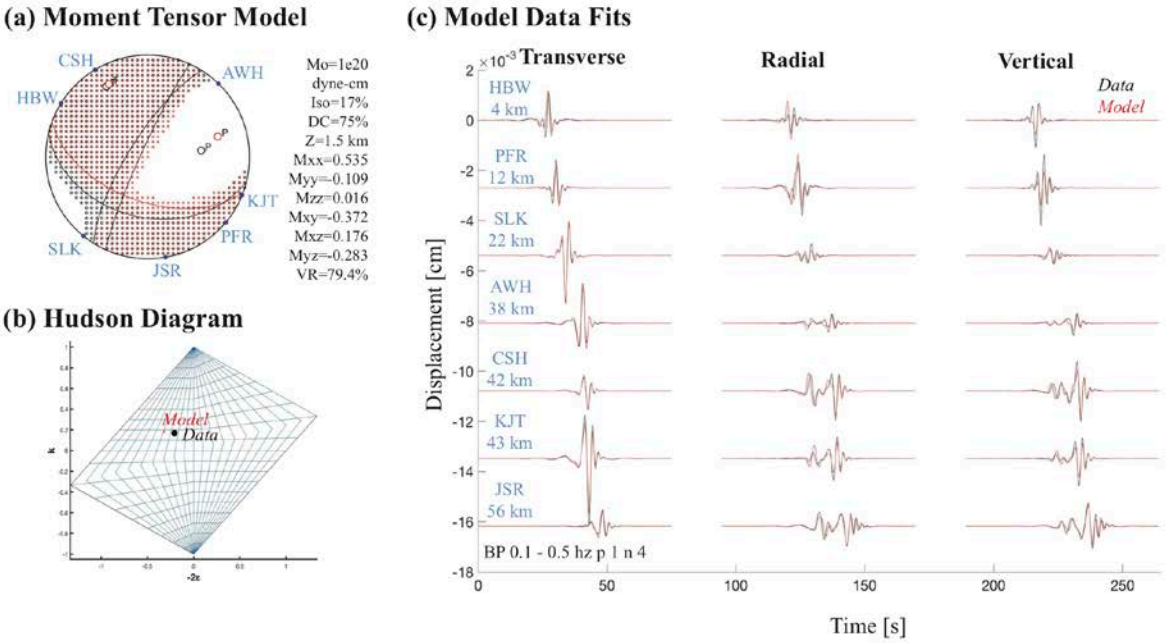

Figure 22: Synthetic iVEA result for the 7 station Geysers geometry and M2.87 earthquake (source parameters from Boyd et al., 2018). *Synthetic 1-D Green's Functions used for inversion were developed for REF1.0 at the surface-surface paths and then converted to earthquake dislocation buried Green's Functions at z=1.5 km. The 0.1 to 0.5 Hz passband was used.*

Real Data; Synthetic 1-D GFs

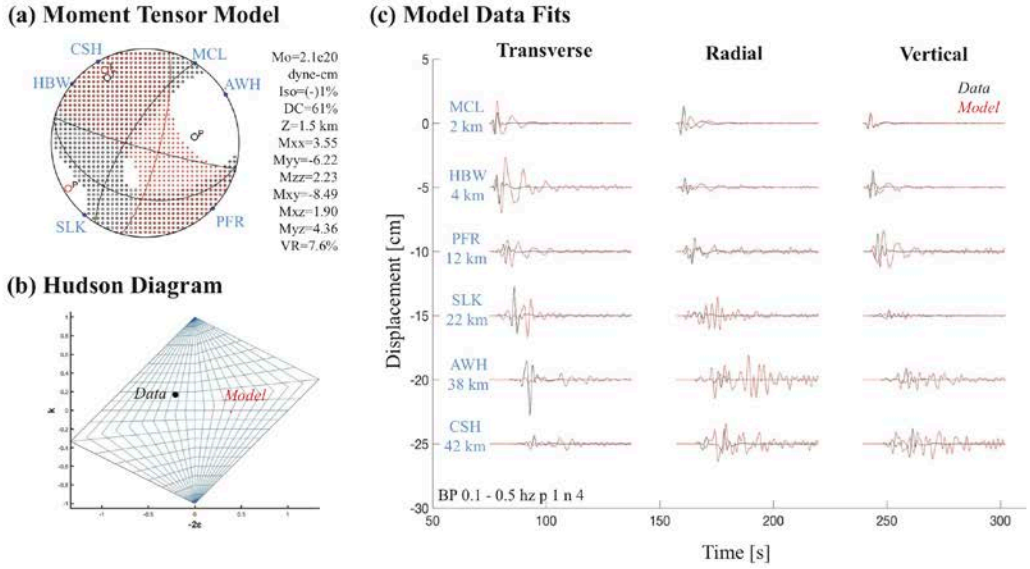

Figure 23: iVEA result for the 6 station Geysers geometry and M2.87 earthquake using real earthquake records. *Synthetic 1-D Green's Functions used for inversion were developed for REF1.0 at the surface-surface paths and then converted to earthquake dislocation buried Green's Functions at z=1.5 km. The 0.1 to 0.5 Hz passband was used.*

Next we perform inversions using the derived NCT. First we perform the iVEA in the 0.1 to 0.3 Hz passband (Figure 24). It is possible to fit the data at the 66% level, however the derived mechanism deviates significantly than the control solution for the event from Boyd et al. (2018). This is a discouraging result. Testing the 0.3 to 0.5 Hz passband (Figure 25) we find that it is possible to fit the data at 41% and a mechanism consistent with the control mechanism is obtained, a little more promising. These two cases used the coherency NCT. Figure 26 and 27 compare the results for the same bands using the deconvolution NCTs. The results using the deconvolution NCTs are very similar indicating that the difference in the NCT for this case does not lead to substantially different results.

Real Data; Real NCTs

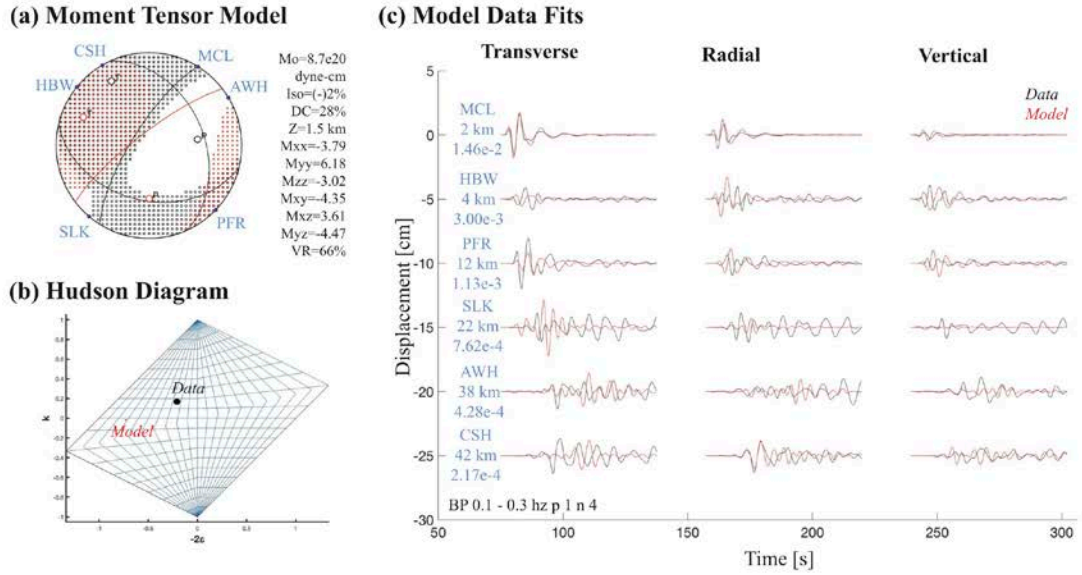

Figure 24: iVEA Coherency result for the M2.87 earthquake and 6 station Geysers geometry using real earthquake records. *Ambient NCTs were developed over 6 months and then converted to earthquake dislocation buried Green's Functions at z=1.5 km using the surface wave dispersion information for a simple 1-D velocity model (see Figure 2). BP 0.1-0.3 p 1 n 4. VR=66%. See previous figure for axis descriptions.*

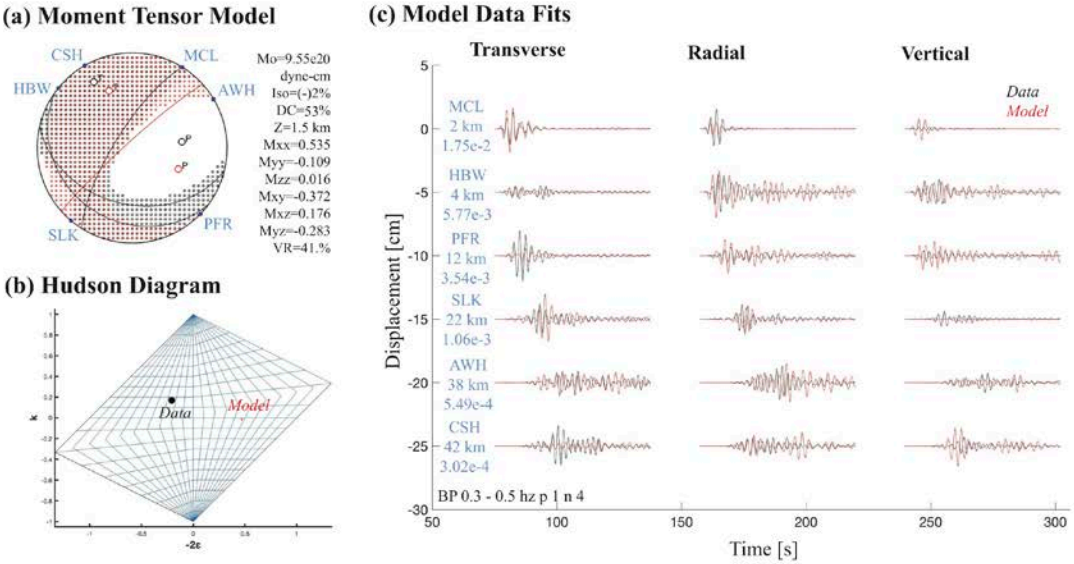

Figure 25: iVEA Coherency result for the M2.87 earthquake and 6 station Geysers geometry using real earthquake records. *Ambient NCTs were developed over 6 months and then converted to earthquake dislocation buried Green's Functions at z=1.5 km using the surface wave dispersion information for a simple 1-D velocity model (see Figure 2). BP 0.3-0.5 p 1 n 4. VR=42%. See previous figure for axis descriptions. Difference between Figure 24 and 25 is the frequency passband.*

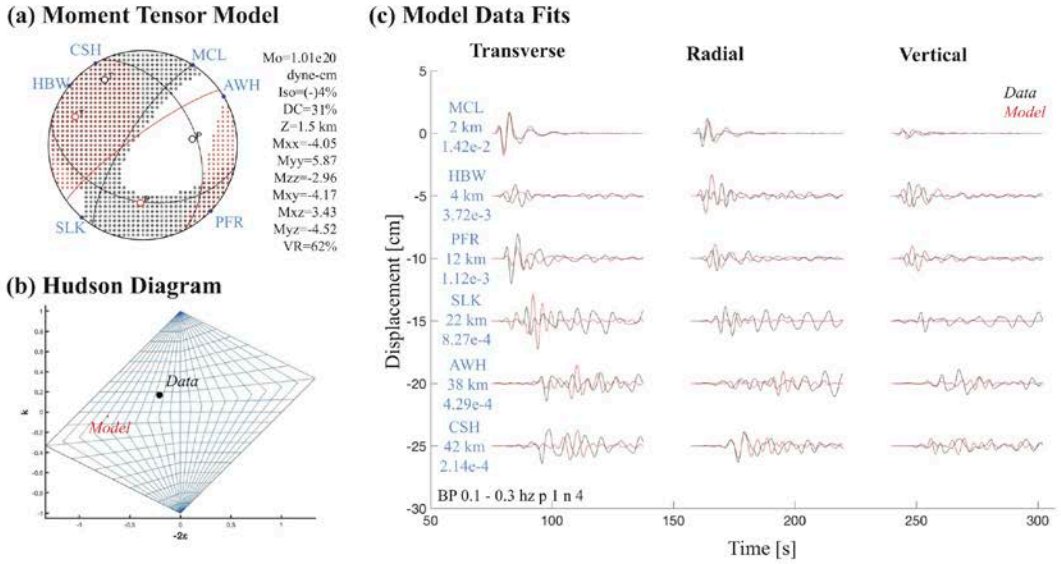

Figure 26: iVEA Deconvolution result for the M2.87 earthquake and 6 station Geysers geometry using real earthquake records. *Ambient NCTs were developed over 6 months and then converted to earthquake dislocation buried Green's Functions at z=1.5 km using the surface wave dispersion information for a simple 1-D velocity model (see Figure 2). BP 0.1-0.3 p 1 n 4. VR=62%. See previous figure for axis descriptions.*

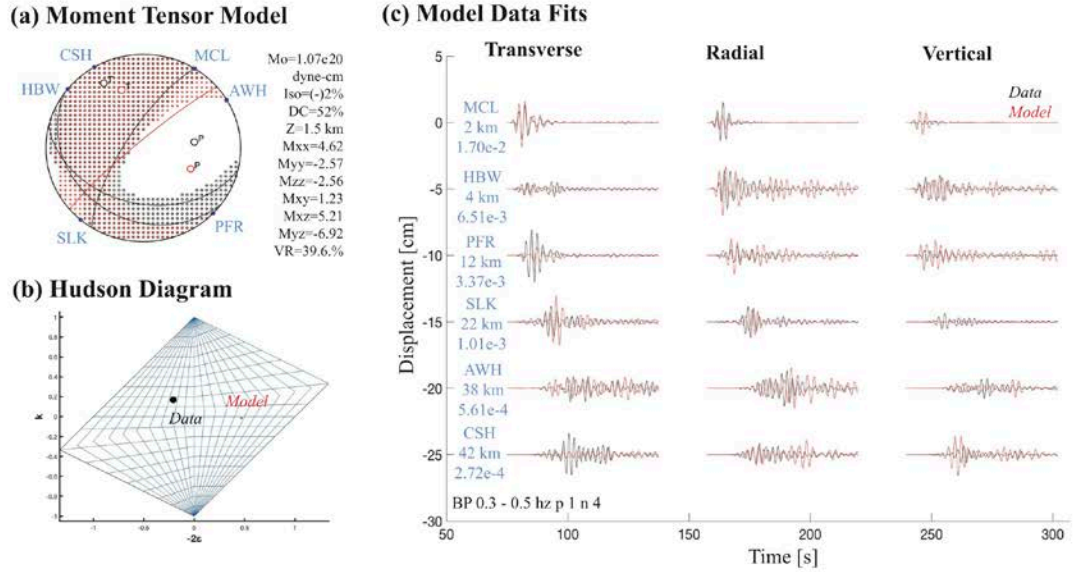

Figure 27: iVEA Deconvolution result for the M2.87 earthquake and 6 station Geysers geometry using real earthquake records. *Ambient NCTs were developed over 6 months and then converted to earthquake dislocation buried Green's Functions at z=1.5 km using the surface wave dispersion information for a simple 1-D velocity model (see Figure 2). BP 0.3-0.5 p 1 n 4. VR=40%. See previous figure for axis descriptions. Difference between Figure 26 and 27 is the frequency passband.*

4.2.5 Discussion and Conclusions

The tests of the iVEA method using synthetic NCT indicates that the iVEA method is capable of retrieving the full moment tensor accurately, but the best results are for a wide band from 0.1 to 0.5 Hz. As the recovery of real NCT depends on operating on the dominant noise band, and is subject to the non-uniformity of the ambient noise sources there is noise in the NCT which affects the iVEA inversion results. The frequency range of application needs to be carefully chosen. Microearthquake sources (like those modeled in this study through iVEA) radiate energy at high frequencies (f>1-50 Hz) significantly above background noise at local distances, but not at lower frequencies (f<0.1 Hz). The primary and secondary microseism bands are generated by ocean-solid earth interaction offshore and radiate energy in the 0.05 – 0.5 Hz band. Hence there is a narrow overlapping band where the micro-earthquake of interest has energy and where ambient noise sources provide sufficient energy to compute NCTs for the station pairs that were used. This would be much easier for a large earthquake case where seismic data is of higher energy and signal-to-noise in the 0.05 – 0.5 Hz. However, to accurately recover the NCT at these lower frequencies requires more data to stack and is just as reliant on the assumed uniform distribution of noise sources. Extending the applicaton to larger distance and lower frequencies is the focus of ongoing work.

5. CONCLUSIONS

We have investigated the feasibility of using ambient noise NCT as Green functions in seismic moment tensor inversion. To do this we employed theoretical unit-force surface-focus Green's functions applying the source depth and spatial derivative corrections outlined by Denolle et al. (2013). The results show that with these corrections unit-force Green's functions can be effectively converted to depth-focus dislocation source Green's functions using fundamental mode theory, and can be used effectively to invert for the moment tensor. These tests evaluate only the noise associated with the approximate nature of the corrections. This "noise" does introduce errors in the recovered moment tensors that have approximately the same magnitude as errors in traditional theoretical Green's function inversions of real data. The analysis shows that the source depth and derivative corrections are dependent on the magnitude of the correction and not surprisingly shallower depths perform better. These tests indicate that errors of +-15% in the isotropic component and +-30-40% in the CLVD component arise from the approximate nature of the source-depth and spatial derivative corrections.

To test the approach using real data we chose for study a small earthquake located at the Geysers in northern California because of independent control of the moment tensor solution for the event, its location very close to a recording station (AL4) and prior work on investigating the recovery of the NCT. As a part of this work we developed a work flow for estimating NCT using both the coherency and deconvolution methods, and found that stable NCT in the 0.1 to 0.5 Hz passband could be recovered with about 180 days of stacking. The stability of the NCT was assessed by quantifying the correlation coefficient change of the NCT as additional days were stacked in. In addition, for some paths comparison of the NCT with theoretical 1D Green's functions indicates the NCT is recovered well. Other paths show that the NCT are much more complex than the corresponding NCT indicating influence of 3D wave propagation. While the NCT stabilized with a 180 day stack in some instances agreed with 1D Green's functions they still may be biased due to non-stationarity of the ambient noise sources. This is another form of noise which can affect the use of NCT in seismic moment tensor estimation.

The results applying the iVEA to the Geysers earthquake data is somewhat disappointing. For the event there is a narrow overlap between the band of the small earthquake with signals adequately above noise and the microseism excitation band used to develop the NCT. We found large errors in the mechanism recovered moment tensor using a lower frequency passband of 0.1 to 0.3 Hz. In testing other passbands we did find that the relatively narrow 0.3 to 0.5 Hz passband was able to recover the correct solution. It is noted that the iVEA performed significantly better than theoretical Green's functions in this passband.

At this point the research does not indicate that it will be possible to apply a pure NCT based moment tensor inversion, though more work with larger earthquakes is being carried out with an effort to extend the NCT to lower frequencies. Another application which should be investigated is the use of the NCT Green's functions in hybrid inversions where theoretical Green's functions are used for paths where they are appropriate and the NCT Green's functions are used for paths that have to be discarded due to 3D wave propagation, multipathing, blocking and propagation through basin structures that greatly affect the observed waveform. Our continuing efforts are investigating the possibility of using a lower frequency passband for larger earthquakes using NCT stacked over a longer period of time, and the investigation of the feasibility and possible benefit of a hybrid approach.

References

Aki, K., and P. G. Richards (2002). *Quantitative seismology*. Second Edition, University Science Books, Sausalito, California, ISBN 0-935702-96-2, 700p.

Alvizuri, C., V. Silwal, L. Krischer, and C. Tape (2018). Estimation of full moment tensors, including uncertainties, for nuclear explosions, volcanic events, and earthquakes. *J. Geophys. Res., 123,* 5099-5119, doi:10.1029/2017JB015325.

Bensen, G. D., M. H. Ritzwoller, M. P. Barmin, A. L. Levshin, F. Lin, M. P. Moschetti, N. M. Shapiro, and Y. Yang (2007). Processing seismic ambient noise data to obtain reliable broad-band surface wave dispersion measurements, *Geophys. J. Int., 169*(3), 1239-1260.

Boyd, O. S., D. S. Dreger, V. H. Lai, and R. Gritto (2015). A Systematic Analysis of Seismic Moment Tensor at The Geysers Geothermal Field, California, *Bull. Seis. Soc. Am., 105*, doi:10.1785/0120140285.

Boyd, O. S., D. S. Dreger, R. Gritto, and J. Garcia (2018). Analysis of seismic moment tensors and in-situ stress during Enhanced Geothermal System development at The Geysers geothermal field, California, *Geophys. J. Int., 215*, 1483–1500, doi:10.1093/gji/ggy326

Brenguier, F., N. M. Shapiro, M. Campillo, V. Ferrazzini, Z. Duputel, O. Coutant, and A. Nercessian (2008a). Towards forecasting volcanic eruptions using seismic noise, *Nature Geoscience, 1*, 126-130.

Brenguier, F., M. Campillo, C. Hadziioannou, N. M. Shapiro, R. M. Nadeau, and E. Larose (2008b). Postseismic relaxation along the San Andreas Fault at Parkfield from continuous seismological observations, *Science, 321,* 1478-1481.

Campillo, M., and A. Paul (2003). Long-range correlations in the diffuse seismic coda, *Science*, *299*(5606), 547-549.

Chiang, Andrea (2015). Investigating Source Processes of Isotropic Events, Ph.D. Dissertation, University of California, Berkeley, 113pp.

Chiang, A., D. S. Dreger, S. R. Ford, and W. R. Walter (2014). Source characterization of underground explosions from combined moment tensor and first motion analysis, *Bull. Seis. Soc. Am., 104*, 1587-1600.

Chiang, A., D. S. Dreger, S. R. Ford, W. R. Walter, and S. H. Yoo (2016). Moment tensor analysis of very shallow sources, *Bull. Seis. Soc. Am., 106,* 2436-2449, doi:10.1785/0120150233.

Chiang, A., G. A. Ichinose, D. S. Dreger, S. R. Ford, E. Matzel, S. Myers, and W. R. Walter (2018). Moment tensor source-type analysis for the Democratic People's Republic of Korea declared nuclear explosions (2006-2017) and 3 September 2017 collapse event, *Seis. Res. Lett., 89,* 2152-2165, doi:10.1785/0220180130.

Covellone, B.M. and B. Savage (2012). A quantitative comparison between 1D and 3D source inversion methodologies: Application to the Middle East, *Bull. Seis. Soc. Am, 102,* 2189-2199.

Curtis, A., P. Gerstoft, H. Sato, R. Snieder, and K. Wapenaar (2006). Seismic interferometry—Turning noise into signal, *The Leading Edge*, *25*(9), 1082-1092.

Denolle, M. A., E. M. Dunham, G. A. Prieto, and G. C. Beroza (2013). Ground motion prediction of realistic earthquake sources using the ambient seismic field, *J. Geophys. Res., 118*, 2102-2118.

Denolle, M. A., E. M. Dunham, G. A. Prieto, and G. C. Beroza (2014a). Strong ground motion prediction using virtual earthquakes, *Science*, *343*(6169), 399-403.

Denolle, M. A., H. Miyake, S. Nakagawa, N. Hirata, and G. C. Beroza (2014b). Long-period seismic amplification in the Kanto Basin from the ambient seismic field, *Geophys. Res. Lett*, *41*, 2319-2325.

Dreger, D. S., and D. V. Helmberger (1993). Determination of source parameters at regional distances with single station or sparse network data, *J. Geophys. Res., 98*, 8107-8125.

Dreger, D., and B. Woods (2002). Regional distance seismic moment tensors of nuclear explosions, *Tectonophysics, 356*, 139-156.

Dreger, D. S., S. R. Ford, and W. R. Walter (2008). Source analysis of the Crandall Canyon, Utah, mine collapse, *Science, 321*, 217.

Dreger, D. S. (2018). Berkeley Seismic Moment Tensor Method, Uncertainty Analysis, and Study of Non-double-couple Seismic Events, in *Moment Tensor Solutions*, S. D'Amico (ed.), Springer International Publishing, 17pp.

Duputel, Z., L. Rivera, H. Kanamori, and G. Hayes (2012). W phase source inversion for moderate to large earthquakes (1990–2010), *Geophys. J. Int.*, *189*(2), 1125-1147.

Dziewonski, A. M., T.-A. Chou and J. H. Woodhouse (1981). Determination of earthquake source parameters from waveform data for studies of global and regional seismicity, *J. Geophys. Res., 86*, 2825-2852, doi:10.1029/JB086iB04p02825.

Ekström, G., M. Nettles, A.M. Dziewonski (2012). The global CMT project 2004–2010: Centroid-moment tensors for 13,017 earthquakes, *Phys. Earth Planet. Int., 200*, 1-9.

Ford, Sean Ricardo (2008). Isotropic Sources and Attenuation Structure: Nuclear Tests, Mine Collapses and Q, Ph.D. Dissertation, University of California, Berkeley, 150pp.

Ford, S., D. Dreger and W. Walter (2008). Source Characterization of the August 6, 2007 Crandall Canyon Mine Seismic Event in Central Utah, *Seis. Res. Lett., 79*, 637-644.

Ford, S. R., D. S. Dreger and W. R. Walter (2009a). Identifying isotropic events using a regional moment tensor inversion, *J. Geophys. Res., 114*, B01306, doi:10.1029/2008JB005743.

Ford, S. R., D. S. Dreger, and W. R. Walter, (2009b). Source Analysis of the Memorial Day Explosion, Kimchaek, North Korea, *Geophys. Res. Lett., 36*, L21304.

Ford, S. R., D. S. Dreger and W. R. Walter (2010). Network sensitivity solutions for regional moment tensor inversions, *Bull. Seis. Soc. Am., 100*, 1962-1970.

Ford., S. R., W. R. Walter and D. S. Dreger (2012). Event discrimination using regional moment tensors with teleseismic-P constraints, *Bull. Seis. Soc Am., 102*, 867-872, doi:10.1785/0120110227.

Gilbert, F. (1973). A discussion on the measurement and interpretation of changes of strain in the Earth-Derivation of source parameters from low-frequency spectra, *Phil. Trans. R. Soc. Lond. A, 274,* 369-371.

Guilhem, A., L. Hutchings, D. S. Dreger, and L. R. Johnson (2014). Moment tensor inversions of M ~ 3 earthquakes in the Geysers geothermal fields, California, *J. Geophys. Res., 119,* 2121-2137, doi:10.1002/2013JB010271.

Hadziioannou, C., E. Larose, O. Coutant, P. Roux and M. Campillo (2009). Stability of monitoring weak changes in multiply scattering media with ambient noise correlation: Laboratory experiments, *J. Acoust. Soc. Am, 125,* 3688-3695.

Heeszel, D. S., D. A. Wiens, A. A. Nyblade, S. E. Hansen, M. Kanao, M. An, and Y. Zhao (2013). Rayleigh wave constraints on the structure and tectonic history of the Gamburtsev Subglacial Mountains, East Antarctica, *J. Geophys. Res., 118,* 2138-2153.

Herrmann, R. B. (1978). *Computer Programs in Earthquake Seismology,* St. Louis University, St. Louis, MO.

Herrmann, R. B. (2013). Computer programs in seismology: An evolving tool for instruction and research, *Seis. Res. Lett., 84,*1081-1088, doi:10.1785/0220110096.

James, S. R., H. A. Knox, R. E. Abbott, and E. J. Screaton (2017). Improved moving window cross-spectral analysis for resolving large temporal seismic velocity changes in permafrost, *Geophys. Res. Lett., 44,* 4018-4026.

Johnson, L. R., and E. L. Majer (2017). Induced and triggered earthquakes at The Geysers geothermal reservoir, *Geophys. J. Int., 209,* 1221-1231, doi:10.1093/gji/ggx082.

Jost, M. L., and R. B. Herrmann (1989). A student's guide to and review of moment tensors, *Seis. Res. Lett., 60,* 37-57.

Julian, B. R., A. D. Miller, and G. R. Foulger (1998). Non-double-couple earthquakes 1. Theory, *Rev. Geophys., 36,* 525-549.

Kwak, S., S. G. Song, G. Kim, C. S. Cho, and J. S. Shin (2017). Investigating the capability to extract impulse response functions from ambient seismic noise using a mine collapse event, *Geophys Res. Lett., 44*(19), 9653-9662.

Lawrence, J. F., and G. A. Prieto (2011). Attenuation tomography of the western United States from ambient seismic noise, *J. Geophys. Res, 116*(B6), doi:10.1029/2010JB007836.

Lin, F. C., D. Li, R. W. Clayton, and D. Hollis (2013). High-resolution 3D shallow crustal structure in Long Beach, California: Application of ambient noise tomography on a dense seismic array, *Geophysics*, *78*(4), Q45-Q56.

Lin, F. C., M. P. Moschetti, and M. H. Ritzwoller (2008). Surface wave tomography of the western United States from ambient seismic noise: Rayleigh and Love wave phase velocity maps, *Geophys. J. Int., 173*(1), 281-298.

Majer, E. L., and T. V. McEvilly (1979). Seismological investigations at The Geysers geothermal field, *Geophysics*, *44*(2), 246-269.

Majer, E. L., and J. E. Peterson (2007). The impact of injection on seismicity at The Geysers, California Geothermal Field, *Int. J. Rock Mech. Min. Sci., 44*(8), 1079-1090.

Miller, A. D., B. R. Julian, and G. R. Foulger (1998). Three-dimensional seismic structure and moment tensors of non-double-couple earthquakes at the Hengill–Grensdalur volcanic complex, Iceland, *Geophys. J. Int.*, *133*(2), 309-325.

Minson, S. and D. Dreger (2008). Stable Inversions for Complete Moment Tensors, *Geophys. J. Int.*, *174*, 585-592.

Nayak, A., and D. S. Dreger (2014). Moment tensor inversion of seismic events associated with the sinkhole at Napoleonville Salt Dome, Louisiana, *Bull. Seis. Soc. Am.*, *104*, 1763-1776.

Nayak, A. and D. S. Dreger (2015). Source-type Specific Inversion of Moment Tensors, *Bull. Seis. Soc. Am. 105*, doi:10.1785/0120140334.

Nayak, A., T. Taira, D. S. Dreger, and R. Gritto (2017). Empirical Green's Tensor retrieved from Ambient Noise Cross-Correlations at The Geysers Geothermal Field, Northern California, *Geophys. J. Int.*, *213*, 340-369, doi:10.1093/gji/ggx534.

Nayak, A., and D. S. Dreger (2018). Source inversion of seismic events associated with the sinkhole at Napoleonville Salt Dome, Louisiana using a 3D velocity model, *Geophys. J. Int.*, *214*, 1808-1829, doi:10.1093/gji/ggy202/5000169.

Oppenheimer, D. H. (1986). Extensional tectonics at The Geysers geothermal area, California, *J. Geophys. Res.*, *91*(B11), 11463-11476.

Pasyanos, M. E., D. S. Dreger, and B. Romanowicz (1996). Towards Real-Time Determination of Regional Moment Tensors, *Bull. Seis. Soc. Am.*, *86*, 1255-1269.

Prieto, G. A., and G. C. Beroza (2008). Earthquake ground motion prediction using the ambient seismic field, *Geophys. Res. Lett.*, *35*, doi:10.1029/2008GL034428.

Prieto, G. A., J. F. Lawrence, A. I. Chung, and M. D. Kohler (2010). Impulse response of civil structures from ambient noise analysis, *Bull. Seis. Soc. Am.*, *100*(5A), 2322-2328.

Prieto, G. A., M. Denolle, J. F. Lawrence, and G. C. Beroza (2011). On amplitude information carried by the ambient seismic field, *Comptes Rendus Geoscience*, *343*(8-9), 600-614.

Sager, K., C. Boehm, L. Ermert, L. Krischer, and A. Fichtner (2018). Sensitivity of seismic noise correlation functions to global noise sources, *J. Geophys. Res, 123*, 6911–6921 doi:10.1029/2018JB016042.

Seats, K. J., J. F. Lawrence, and G. A. Prieto (2012). Improved ambient noise correlation functions using Welch′ s method, *Geophys. J. Int.*, *188*(2), 513-523.

Shapiro, N. M., and M. Campillo (2004). Emergence of broadband Rayleigh waves from correlations of the ambient seismic noise, *Geophys. Res. Lett.*, *31*(7), doi:10.1029/2004GL019491.

Sheng, Y., M. Denolle, and G. C. Beroza (2017). Multicomponent C3 Green's Functions for Improved Long-Period Ground-Motion Prediction, *Bull. Seis. Soc. Am.*, *107*(6), 2836-2845.

Snieder, R. (2004). Extracting the Green's function from the correlation of coda waves: A derivation based on stationary phase, *Physical Review E, 69*(4), 046610.

Stehly, L., and P. Boué, (2017). On the interpretation of the amplitude decay of noise correlations computed along a line of receivers, *Geophys. J. Int.*, *209*(1), 358-372.

Tsai, V. C. (2011). Understanding the amplitudes of noise correlation measurements, *J. Geophys. Res., 116,* B09311, doi:10.1029/2011JB008483.

Vavryčuk, V. (2015). Inversion for the composite moment tensor, *Bull. Seis. Soc. Am, 105*(6), 3024-3035.

Vavryčuk, V. (2018). Seismic moment tensors in anisotropic media: A review, in *Moment Tensor Solutions,* D'Amico S. (ed.), Springer Natural Hazards, Springer, Cham, doi:10.1007/978-3-319-77359-9_2.

Viens, L., A. Laurendeau, L. F. Bonilla, and N. M. Shapiro (2014). Broad-band acceleration time histories synthesis by coupling low-frequency ambient seismic field and high-frequency stochastic modelling, *Geophys. J. Int., 199*(3), 1784-1797.

Viens, L., H. Miyake, and K. Koketsu (2015). Long-period ground motion simulation of a subduction earthquake using the offshore-onshore ambient seismic field, *Geophys. Res. Lett., 42*(13), 5282-5289.

Viens, L., M. Denolle, H. Miyake, S. I. Sakai, and S. Nakagawa (2017). Retrieving impulse response function amplitudes from the ambient seismic field, *Geophys. J. Int., 210*(1), 210-222.

Walter, F., J. F. Clinton, N. Deichmann, D. S. Dreger, S. E. Minson, and M. Funk (2009). Moment tensor inversions of icequakes on Gornergletscher, Switzerland, *Bull. Seis. Soc. Am., 99*(2A), 852-870.

Wapenaar, K., D. Draganov, R. Snieder, X. Campman, and A. Verdel (2010). Tutorial on seismic interferometry: Part 1—Basic principles and applications, *Geophysics, 75*(5), 75A195-75A209, doi:10.1190/1.3457445.

Zhan, Z., V. C. Tsai, J. M. Jackson, and D. Helmberger (2013). Ambient noise correlation on the Amery Ice Shelf, east Antarctica, *Geophys. J. Int., 196*(3), 1796-1802.

DISTRIBUTION LIST

DTIC/OCP
8725 John J. Kingman Rd, Suite 0944
Ft Belvoir, VA 22060-6218 1 cy

AFRL/RVIL
Kirtland AFB, NM 87117-5776 1 cy

Official Record Copy
AFRL/RVBYE/Dr. Frederick Schult 1 cy

This page is intentionally left blank.